

1

2 **Towards an objective assessment of climate multi-model** 3 **ensembles. A case study : the Senegalo-Mauritanian upwelling** 4 **region**

5 Juliette Mignot¹, Carlos Mejia¹, Charles Sorrow¹, Adama Sylla^{1,2}, Michel Crépon¹ and Sylvie
6 Thiria^{1,3}.

7 ¹ IPSL-LOCEAN, SU/IRS/CNRS/MNHN, Paris, France

8 ² LPAO-SF, ESP, UCAD, Dakar, Sénégal

9 ³ UVSQ, F-78035, Versailles, France

10 *Correspondence to:* Juliette Mignot (Juliette.mignot@locean-ipsl.upmc.fr)

11 **Abstract.** Climate simulations require very complex numerical models. Unfortunately, they
12 typically present biases due to parameterizations, choices of numerical schemes, and the
13 complexity of many physical processes. Beyond improving the models themselves, a way to
14 improve the performance of the modeled climate is to consider multi-model combinations. In the
15 present study, we propose a method to select the models that yield a multi-model ensemble
16 combination that efficiently reproduces target features of the observations. We used a neural
17 classifier (Self-Organizing Maps), associated with a multi-correspondence analysis to identify the
18 models that best represent some target climate property. We can thereby determine an efficient
19 multi-model ensemble. We illustrated the methodology with results focusing on the mean sea
20 surface temperature seasonal cycle on the Senegalo-Mauritanian region. We compared 47 CMIP5
21 model configurations to available observations. The method allows us to identify a subset of
22 CMIP5 models able to form an efficient multi-model ensemble. The future decrease of the
23 Senegalo-Mauritanian upwelling proposed in recent studies is then revisited using this multi-
24 model selection.

25

26

27 **1- Introduction**

28 In this study, we present a methodology aimed at selecting a coherent sub-ensemble of the
29 models involved in the Climate Model Intercomparison Project, Phase 5 (CMIP5) that best
30 represents specific observed characteristics. While the future evolution of the global climate is
31 subject to great changes and great uncertainty (Collins et al., 2014), the most common way to
32 predict the evolution of the climate is to run climate models that include fully coupled
33 atmosphere-ocean-cryosphere-biosphere modules. Due to their low resolution, and the fact that
34 they use different parameterizations of the physics, numerical schemes and sometimes include or
35 neglect different processes, these models have some marked biases in specific regions. They also
36 have different responses to an imposed increase of atmospheric greenhouse gases, which partly
37 explain their mean climate biases. This variety of models allows us to assess the uncertainty of
38 present climate representation when compared to observations and, by studying their dispersion,
39 to roughly estimate the uncertainty of the response to future climate change.

40 For several generations of climate models, it has been shown that for a large variety of
41 variables the multi-model average generally agrees better with observations of present day
42 climate than any single model (Lambert and Boer, 2001; Phillips and Gleckler, 2006; Reichler
43 and Kim, 2008; Santer et al., 2009; Tebaldi and Knutti, 2007). Several studies also suggest that
44 the most reliable climate projection is given by a multi-model averaging (Knutti et al., 2010),
45 rather than, for example, averaging different projections performed with a single model run with
46 different initial conditions. This result relies on the assumption that if choices of
47 parameterizations or specific numerical schemes are made independently for each model, then the
48 errors might at least partly compensate, resulting in a multi-model average that is more skillful
49 than its constitutive terms (Tebaldi and Knutti, 2007). The significant gain in accuracy can be
50 explained by the fact that the errors specific to each model compensate each other in the
51 averaging procedure used to build the multi-model mean. However, the number of GCMs
52 available for climate change projections is increasing rapidly. For example, the CMIP5 archive
53 (Taylor et al., 2012), which was used for the fifth IPCC Assessment Report (Stocker et al., 2013),
54 contains outputs from 61 different GCMs and 70 contributions are expected for CMIP6. It thus
55 becomes possible - and probably needed - to select and/or weight the models constituting such an
56 average. Recent work has suggested that weighting the multi-model averaging procedure could
57 help to reduce the spread and thus uncertainty of future projections. Such an approach has been
58 applied extensively to the issue of climate sensitivity (Fasullo and Trenberth, 2012; Gordon et al.,

59 2013; Huber and Knutti, 2012; Tan et al., 2016). Valuable improvement of model selection has
60 also been found in studies of the carbon cycle (Cox et al., 2013; Wenzel et al., 2014), the
61 hydrological cycle (Deangelis et al., 2015; O’Gorman et al., 2012), the Antarctic atmospheric
62 circulation (Son et al., 2010; Wenzel et al., 2016), extratropical atmospheric rivers (Gao et al.,
63 2016), atmospheric and ocean heat transports (Loeb et al., 2015), European temperature
64 variability (Stegehuis et al., 2013) and temperature extremes (Borodina et al., 2017).

65 The present paper works towards the elaboration of an objective method to select models
66 according to their performance for a specific phenomenon. Here, we use the Senegalo-
67 Mauritanian upwelling area as a case study to construct an efficient climate multi-model
68 combination together with its related confidence interval in order to anticipate the effect of
69 climate warming by the end of the century in this region. The Senegalo-Mauritanian upwelling
70 has been the focus of increasing attention over recent years. The very productive waters
71 associated with the upwelling have a strong economic impact on fisheries in Senegal and
72 Mauritania, and a crucial societal importance for local populations. It is therefore important to
73 predict the evolution of the dynamics and the physics of the upwelling in the forthcoming
74 decades, due to the effect of climate warming and its consequences on biological productivity,
75 which may impact the fisheries. The Senegalo-Mauritanian upwelling lies at the southern end of
76 the Canarian upwelling system, which has a relatively weak seasonality and is maximum in
77 summer. On the contrary, the Senegalo-Mauritanian upwelling presents a well-marked seasonal
78 variability. Its intensity is stronger in boreal winter and it disappears in summer with the
79 northward progression of the ITCZ. Due to the enrichment of the sea surface layers with
80 nutrients upwelled from deep layers, it drives an important phytoplankton bloom that is observed
81 on ocean color satellite images (Demarcq and Faure, 2000; Farikou et al., 2015). The maximum
82 intensity of this bloom occurs in March-April (Farikou et al., 2015; Faye et al., 2015; Ndoye et
83 al., 2014). Its important seasonal cycle is also associated with mesoscale patterns whose
84 variability has been recently studied by several oceanographic campaigns (Capet et al., 2017;
85 Faye et al., 2015; Ndoye et al., 2014) and theoretical work (Sirven et al., 2019). Sylla et al., 2019
86 have recently shown that the intensity of the SST seasonal cycle along the coast of Senegal and
87 Mauritania was a good marker of the upwelling in this specific region in climate models. They
88 have used this index together with other more dynamical indices to predict that the upwelling will
89 decrease by about 10% of its present-day amplitude by the end of the 21st century. Nevertheless,

90 their study also highlighted a large uncertainty due to model biases in this region. The method we
91 have developed selects a subset of the CMIP5 ensemble based on the capability of the climate
92 models to reproduce the SST seasonal cycle observed during the historical period in key sub-
93 regions. These sub-regions are identified by a neural classifier. The method leads us to rank the
94 different models and to determine an efficient multi-model combination for the analysis of the
95 Senegalo-Mauritanian upwelling and projections of its behavior in global warming conditions.

96 The paper is structured as follows: section 2 presents the different climate models and the
97 climatological observations used in the study, together with the region of interest. The
98 classification method is described in section 3 and applied to the extended region. Section 4
99 presents a qualitative analysis able to group the different climate models in clusters presenting
100 similar performances. Section 5 investigates the results of the method applied over a smaller area,
101 more focused over the upwelling region. Section 6 uses the two multi-model clusters defined in
102 sections 4 and 5 respectively to tentatively predict the representation of the Senegalo-Mauritanian
103 upwelling changes under global warming. Conclusions are given in section 7.

104

105 **2- Climate Models and region of interest**

106 **2.1 Data**

107 This study is based on the CMIP5 (Coupled Model Inter-comparison Project Phase 5) database.
108 We use the output of 47 simulations listed in Table 1. The models are evaluated over the
109 historical period defined as [1975-2005] by comparing their output to observations. The mean
110 seasonal cycle of SST anomalies over this period is constructed for each model grid point as the
111 difference between the monthly mean temperature and the mean annual temperature. When
112 several members of historical simulations are available for a specific model configuration, they
113 are averaged together. However, this has practically no impact on the estimated mean seasonal
114 cycle (not shown). The mean climatological cycle of the CMIP5 models under study is evaluated
115 against the Extended Reconstructed Sea Surface Temperature data set (ERSST- v3b, Smith et al.,
116 2008), averaged over the same time period. This data set was produced by NOAA at 2° spatial
117 resolution. It is derived from the International Comprehensive Ocean–Atmosphere Dataset with
118 missing data filled in by statistical methods. This dataset is used as the target to be reproduced

119 and is denoted "observation field" hereafter. In order to deal with data at the same resolution, all
120 model outputs as well the observation fields were regridded on a 1-degree resolution regular grid
121 prior to analysis. A previous study (Sylla et al., 2019) has compared the performance of this
122 dataset as compared to the gridded SST data set from the Met Office Hadley Centre HadISST
123 (Rayner, 2003). The main results regarding the future of the upwelling were shown to be
124 independent of the validation dataset primarily because the models' biases and the inter-model
125 differences were much larger than the differences between the validation datasets. The
126 methodological and oceanographic results presented in this study are thus expected to depend
127 only very weakly on the target dataset.

128 In section 6, the model selections are used to characterize the response of the upwelling to
129 climate change. This response is characterized in terms of SST anomalies as well as wind
130 intensity. For wind intensity, the simulated wind stress is compared to the TropFlux reanalysis.
131 This data set combines the ERA-Interim reanalysis for turbulent and long-wave fluxes, and
132 ISCCP (International Satellite Cloud Climatology Project) surface radiation data for shortwave
133 fluxes. This wind stress product is described and evaluated in (Praveen Kumar et al., 2011).

134

135 **2.2 The Senegalo-Mauritanian upwelling region**

136 In this study, we evaluate the ability of the different climate models to represent the Senegalo-
137 Mauritanian upwelling. Following (Sylla et al., 2019), we consider the intensity of the seasonal
138 cycle of the SST anomaly as a marker of the upwelling variability and localization. This variable
139 is shown in [Fig. 1](#) for the eastern tropical Atlantic. This figure confirms that the Senegalo-
140 Mauritanian coast stands out with a very strong seasonal SST cycle as compared to similar
141 latitudes in the open ocean. This results from the cold SST generated by the strong winds
142 occurring in winter. The Senegalo-Mauritanian upwelling is confined in a small region of the
143 order of 100km off the western coast of Africa. It is part of a complex and fine-scale regional
144 circulation system recently revisited by Kounta et al., 2018. Since the grid mesh of most of the
145 climate models is of the order of 1° (~100km), this regional circulation is poorly resolved, which
146 favors a relatively large-scale analysis of the upwelling representation in climate models. The
147 Senegalo-Mauritanian upwelling is also embedded in a large scale oceanic circulation pattern,
148 encompassing the North Equatorial Counter Current flowing eastward in the southern part of the

149 region and the return branch of the subtropical gyre in the northwestern part. Therefore, we firstly
150 study the representation of the SST seasonal cycle intensity in the different climate models over a
151 relatively large region that includes part of the Canary current in the north and the Guinea dome
152 in the south. The so-called “extended region” is defined by a rectangular box extending from
153 9°W to 45°W and from 5°N to 30°N (Fig. 1). In a second step, we will proceed to the same
154 analysis and classification of the models within a much more focused (hereafter zoomed) region,
155 namely [16°W-28°W and 10°N-23°N] (Fig. 1). All the results below will be first shown for the
156 extended region. Comparison with the focused region will be done in section 4.

157 **3 - Comparing observations and models: a methodological approach**

158 The methodology we have developed is based on the ability of the climate models to adequately
159 reproduce the climatology of the seasonal cycle of the SST anomalies as observed during the last
160 three decades in key sub-regions of the studied domain. These key sub-regions are determined
161 from the similarity of their physical and statistical characteristics through an unsupervised
162 classification, which clusters pixels having similar observed seasonal SST climatology. We chose
163 to deal with a neural classifier, the so-called self-organizing map (SOM hereafter) developed by
164 Kohonen, 2013 followed by a Hierarchical Ascendant Clustering (HAC, Jain and Dubes, 1998).
165 This method leads to a dynamically interpretable classification. The SOM determines a vector
166 quantization of the dataset, which compresses the initial dataset into a relatively small number of
167 reference vectors. Doing so allows us to take the non-linearities of the dataset into account and to
168 filter the noise, which can make the classification spurious. This reduced number of dataset
169 vectors enables an HAC to determine the highly non-linear borders between the different SOM
170 clusters. This procedure has been used with success in several studies (Farikou et al., 2015; Jouini
171 et al., 2016; Niang et al., 2003, 2006; Sawadogo et al., 2009). Note that the use of an HAC
172 directly on the initial dataset would not be efficient in the present study because the number of
173 degrees of freedom (here the grid points of the initial domain) is too large for this method to work
174 efficiently. In the present section, we describe the methodology we developed to score the
175 different climate models with respect to the observations. In section 4, we will tentatively group
176 the different climate models into blocks having the same behavior by using a Multiple
177 Correspondence Analysis (MCA).

178

179 3.1 The unsupervised classification method

180 The first step of the methodology was to decompose the selected region in different classes (the
 181 key sub-regions mentioned above) by using a neural network classifier, the so-called SOM
 182 (Kohonen, 2013). This algorithm constitutes a powerful nonlinear unsupervised classification
 183 method. It has been commonly used to solve environmental problems (Hewitson and Crane,
 184 2002; Jouini et al., 2013, 2016; Liu et al., 2006; Reusch et al., 2007; Richardson et al., 2003). The
 185 SOM aims at clustering vectors (here the 12 SST seasonal anomalies) of a multidimensional
 186 database (\mathbf{D}) (here the grid points of the studied domain) into classes represented by a fixed
 187 network of neurons (the SOM map). The self-organizing map (SOM-map) is defined as an
 188 undirected graph, usually a 2D rectangular grid. This graphical structure is used to define a
 189 discrete distance (denoted by δ) between the neurons of the map and thereby identify the shortest
 190 path between two neurons. Moreover, SOM enables the partition of \mathbf{D} in which each cluster is
 191 associated with a neuron of the map and is represented by a prototype that is a synthetic
 192 multidimensional vector (the referent vector \mathbf{w}). Each vector \mathbf{z} of \mathbf{D} is assigned to the neuron
 193 whose referent \mathbf{w} is the closest, in the sense of the Euclidean Norm (EN), and is called the
 194 projection of the vector \mathbf{z} on the map. A fundamental property of a SOM is the topological
 195 ordering provided at the end of the clustering phase: two neurons that are close on the map
 196 represent data that are close in the data space. In other words, the neurons are gathered in such a
 197 way that if two vectors of \mathbf{D} are projected on two “relatively” close neurons (with respect to δ) on
 198 the map, they are similar and share the same properties. The estimation of the referent vectors \mathbf{w}
 199 of a SOM and the topological order is achieved through a minimization process using a learning
 200 data set base, here from the observations. The cost function to be minimized is of the form:

$$J_{SOM}^T(\chi, W) = \sum_{z_i \in \mathbf{D}} \sum_{c \in SOM} K^T(\delta(c, \chi(z_i))) \|z_i - w_c\|^2$$

201 where $c \in SOM$ indices the neurons of the SOM map, χ is the allocation function that assigns
 202 each element z_i of \mathbf{D} to its referent vector $w_{\chi(z_i)}$ and $\delta(c, \chi(z_i))$ is the discrete distance on the
 203 SOM-map between a neuron c and the neuron allocated to observation z_i . K^T a kernel function
 204 parameterized by T (where T stands for “temperature” in the scientific literature dedicated to
 205 SOM) that weights the discrete distance on the map and decreases during the minimization

206 process. At the end of the learning process, the classification can be visualized onto the SOM-
207 map and interpreted in term of geophysics.

208 **3.2 - Classification of the observations**

209 In the present problem we chose to classify the annual cycles of the SST seasonal anomalies
210 observed in the Senegalo-Mauritanian upwelling. The study was made on the “extended region”
211 constituted of $25 \times 36 = 900$ pixels, but this enlarged region covers a part of the African continent
212 and 157 pixels are in fact over land. That means that we have truly 743 ocean pixels to deal with.
213 We consider a time-period of 30 years [1975 to 2005] extracted from the ERSST-V3b database.
214 For a given grid point and a given year and month, the monthly anomaly is the SST of the pixel
215 for which we have subtracted the mean of the considered year. The climatological mean of the
216 anomaly is then computed for each grid point by averaging each climatological month over the
217 30 years. Thus, the learning data set \mathbf{D} is a set of 743 twelve-component vectors \mathbf{z} , each
218 component being the mean monthly anomaly computed as above. We denote “SST seasonal
219 cycle” the vector \mathbf{z} in the following.

220 We used a SOM-map to summarize the different SST seasonal cycles present in the "extended
221 region". We found that 120 prototypes (or neurons) can accurately represent the 743 vectors of \mathbf{D} .
222 This reduction (or vector quantization) is made by using a rectangular SOM-map of 30×4
223 neurons.

224 We then reduced the number of neurons in order to facilitate their interpretation in terms of
225 geophysical processes. For this, we applied a HAC using the Ward dissimilarity (Jain and Dubes,
226 1988). We grouped the 120 neurons of the SOM into a hierarchy that can contain between 1 and
227 120 clusters. Then the different classifications proposed by the HAC were applied to the
228 geographical region: each SST seasonal cycle of each grid point of the region is assigned to a
229 neuron and consequently to a cluster (assignment process), thereby defining the so-called region-
230 clusters. The problem is then to choose a number of clusters that adequately synthesizes the
231 geophysical phenomena over the region. This was done by looking at the different possible
232 classifications and choosing one representing the major characteristics of the upwelling region.
233 In [Fig. 2a](#), we observe that when we partition the SOM in 7 clusters, the associated 7 region-
234 clusters are constituted of contiguous pixels in the geographic map, and that two clusters (6, 7)
235 are within the upwelling region and present a well-marked seasonal cycle. For each region-

236 cluster, we estimated the monthly mean of the SST seasonal cycle and the associated spread
237 captured by the neurons constituting this region-cluster.

238 The typical SST climatological cycles for each region-cluster are presented in [Fig. 2b](#)
239 together with their related error bars. We note that the region-clusters are well identified, their
240 typical climatological annual cycles of SST being well separated. Furthermore, the 7 region-
241 clusters are spatially coherent and have a definite geophysical significance.

242 For the extended region under study, 7 therefore appears to be an adequate cluster
243 number, since this number balances a clear partition of the clusters on the HAC decision tree with
244 a clear physical significance to each region-cluster. The Senegalo-Mauritanian coastal upwelling
245 is associated with clusters 7 and 6. Cluster 2 corresponds to deep tropical waters associated with
246 the equatorial Countercurrent. Cluster 1 corresponds to surface waters of the Gulf of Guinea.
247 Cluster 3 corresponds to the offshore tropical Atlantic, and cluster 5 has extratropical
248 characteristics. Cluster 4 is transition between 3 and 5. As expected, the equatorial regions
249 (clusters 1 and 2) have a very weak seasonal cycle, which increases towards the extratropics
250 (clusters 3 to 5). The upwelling regions (clusters 6 and 7) are characterized by an exceptionally
251 strong seasonal variability.

252

253 **3.3 – Classification of the climate models on the extended upwelling region**

254 The aim is now to find the model(s) that best fit the “observation field”. A heuristic
255 manner is to compare the pattern of the different region-clusters of the CMIP5 models with
256 respect to those of the “observation field” through a sight evaluating process. This kind of
257 approach has been proposed in Sylla et al., 2019, and we indeed immediately see that some
258 models better fit the “observation field” than others. Nonetheless, this method remains very
259 subjective.

260 In the following, we present a more objective approach. We use the previous
261 classification to objectively estimate how each CMIP5 model fits the “observation field” and its
262 seven region-clusters. For this, we projected the SST annual cycle of each CMIP5 model grid
263 point of the extended region onto the SOM learned with the observations (section 3.2) using the
264 assignment procedure described in this section. Each grid point thus corresponds to a cluster of

265 the SOM and is represented on the geographical map by its corresponding color. Doing so, we
266 can represent each CMIP5 model by the geographical pattern of the 7 clusters partitioning the
267 SST seasonal cycle of its grid points. The geographical maps representing the 47 models and
268 their associated clusters are plotted in [Fig. 3](#). This graphical visualization is easier to compare
269 than the original characteristics (amplitude and phase) of the annual cycle at each grid point of a
270 model since each grid point can only take one discrete value among seven. This representation
271 immediately allows identification of the model biases and the models that best reproduce the
272 cluster-regions identified in the observations. A huge amount of information could in principle be
273 extracted from these maps, both from individual modelling groups, to understand the
274 representation of this region by the models and the origins of possible biases, and from experts of
275 the area, to understand the difficulties of the climate models in representing the SST seasonal
276 cycle in this region.

277 For a more quantitative assessment, we counted the number of grid points of a region-
278 cluster for a given CMIP5 model matching the same region-cluster of the “observation field”. We
279 then computed the ratio between that matching number and the number of pixels of the region-
280 cluster of the considered model. That number is noted in the color-bar for each region-cluster in
281 [Fig. 3](#). We denote R_{mi} the ratio for the region-cluster i and the model m , where $i = 1, \dots, 7$ is the
282 number of the region-cluster and $m = 1, \dots, 47$ is the number of the model (see table 1). We note
283 that $R_{mi} \leq 1$. Doing so, each model m is represented by a 7-dimensional vector R_m , each
284 component being the ratio of a region-cluster. We estimated the total skill of a model by
285 averaging the 7 ratios. Note that this procedure gives the same weight to each region-cluster
286 whatever its number of grid points and its proximity with the upwelling region. In the following,
287 the skill is presented as a percentage: the higher the skill, the better the fit. In [Fig. 3](#), the 47
288 CMIP5 models are ranked by their total skill, which is indicated above each panel beside the
289 model name. The model skills are very diverse, ranging from 79% to 28%. This figure also
290 shows that the models presenting the best total skill are also those representing thoroughly the
291 upwelling region. Some models represent the large-scale structure in the eastern tropical Atlantic
292 (region-clusters 3, 4, 5) very well but not the upwelling (33-GISS-E2-R and 34-GISS-E2-R-CC
293 for example). Others represent pretty well the upwelling region-clusters (region-clusters 6 and 7),
294 but not the large-scale structures of the SST seasonality (13-CSIRO-Mk-3-6-0, 6-CMCC-CESM
295 for example). None of these models is ranked among the best models, with a score greater than

296 60%. As indicated above, this representation gives a very synthetic view of the structure of the
297 seasonality of the SST cycle in each of the models, potentially a very useful guide for climate
298 modelers to identify rapidly major biases.

299

300 **4 – Qualitative analysis of the climate models**

301 In order to further progress in the selection of the models, the 47 climate models and the
302 observation field were then analyzed by using a Multiple Correspondence Analysis (MCA in the
303 following). MCA is a multivariate statistical technique that is conceptually similar to principal
304 component analysis (PCA), but applies to categorical rather than continuous data. Similarly as
305 PCA, it provides a way of displaying a set of data in a two-dimensional graphical form.

306 In the following, we apply a MCA analysis to the (47,7) matrix $\mathbf{R} = [R_{mi}]$ whose
307 elements represent the skills of the clusters of the models shown in front of the color bars in Fig.
308 3: the rows m represent the 47 different models, the columns i the 7 region-clusters. The MCA,
309 as the PCA, projects the initial matrix on a new basis in such a way that the new axes are the
310 matrix eigenvectors (PC), the inertia of each axis being the corresponding eigenvalues.
311 According to the theory, the MCA matrix analysis of \mathbf{R} gives $i-1 = 6$ independent PCs. Each
312 model is thus now associated with a 6-dimensional vector on which it has a specific weight. The
313 MCA uses for this analysis the χ^2 distance. In figure 4, we present the projection of the models
314 and the “region clusters” in the plane formed by the two first axes ($x=PC1$ and $y=PC2$) of the
315 MCA. These two axes represent 70 % of the total inertia. Each model is represented by a small
316 circle and each region-cluster by a purple square. We also projected the observation field (green
317 diamond) on that plane. To have a more precise view of the topology, it would be necessary to
318 consider the projection on the 5 other PCs, which represent 30% of the inertia.

319 In the (PC1, PC2) plane, the shorter the distance between two models, the more similar
320 the distribution of their region-cluster skills. Proximity between a model and a region-cluster
321 leads us to affirm that this region-cluster is well represented by that model. Clearly, some models
322 adequately represent the southern part of the extended region (region-clusters 1, 2 or 3), where
323 the SST seasonal cycle is weak, and are very distant from the upwelling regions (region-cluster 6

324 and region-cluster 7) whose large SST cycle is poorly reproduced. In this group of models, one
325 recognizes the model 16-IPSL-CM5A-MR, at the extreme bottom of [Fig. 4](#), close to region-
326 clusters 4 and 5, consistently with [Fig. 3](#). At the other end of this group of models, the model 23-
327 HadCM3 for example is located very close to the region-cluster 1. [Fig. 3](#) indeed shows that most
328 of its grid points over the region of interest have a seasonal cycle resembling the one found in the
329 offshore tropical ocean. Another group of models is located in the center of this plan, thus at an
330 optimal distance of each of the observed regions-clusters, and not far from the overall position of
331 the observations (diamond). We recognize in this group of models those that have a high skill in
332 [Fig. 3](#). The positioning of the observations (green diamond in [Fig. 4](#)) with respect to the models
333 indeed allows selecting those that best represent the observations field. The representation given
334 in [Fig. 4](#) allows understanding the drawback of the different models with respect to the 7 Modes
335 of SST-cycles.

336 As indicated in the introduction, the main objective of the methodology is to select an
337 ensemble of models that represents at best the upwelling behavior with respect to the
338 observations and to use this ensemble to predict the impact of climate change in the Senegalo-
339 Mauritanian upwelling with some confidence. The problem is now to determine a subset of
340 models which has a better skill than Model-All, in other words minimize the distance to the
341 observations. As the number of models is small enough, we chose to cluster them by an HAC
342 according to their projections onto the six axes provided by the MCA, and select the optimal
343 jump in the hierarchical tree (Jain and Dubes, 1988). We recall that the HAC (hierarchical
344 ascending clustering) is a bottom-up algorithm for dataset clustering. The key operation in
345 hierarchical bottom-up clustering is to repeatedly combine the two nearest (according to a certain
346 distance) clusters into a larger cluster. The HAC starts from individuals and combines them
347 according to their similarity (with respect to the chosen distance) to obtain new clusters. The
348 process is repeated up to get one cluster only (the full dataset). This algorithm is visualized
349 through a tree-like diagram, the so-called connection tree or dendrogram: the branches of the
350 connection tree represent the connections between the clusters ([Fig. 5](#)). From [Fig. 5](#), we obtain
351 four homogeneous groups which are well separated (group 1, 2, 3, 4). They are plotted with
352 different colors in [Fig. 4](#). We denote Model-group 1, Model-group 2, Model-group 3, Model-
353 group 4 these multi-model ensembles hereafter. Note that [Fig. 4](#) shows the projection of the
354 individual models on the first two axes of the MCA. The fact that only two axes are shown here

355 can introduce some bias in the visualization and this figure must be considered with some
356 caution.

357 Through MCA+HAC, we thus grouped the models into clusters, using the χ^2 distance,
358 according to their proximity to the observations and their internal similarity. For each group, we
359 computed a multi-model average whose outputs are the mean of the outputs of its different
360 members and we analyzed it according to the same procedure (projection of the SST-seasonal
361 cycle and assignment to a region-cluster) used for each individual model. In addition, we
362 introduced the full multi-model average (Model-All in the following), which is the multi-model
363 ensemble, which averages the 47 CMIP5 model outputs. Model-All was also projected in the
364 MCA plane and it is represented by a red star in [Fig. 4](#). Comparison of the four model-groups
365 with Model-All and the observations are presented in [Fig. 6](#). This figure visually highlights the
366 dominance of Model-group 4 for the reconstruction of the SST seasonal cycles of the different
367 region-clusters for the extended region. This is particularly clear for region-clusters 6 and 7,
368 which are those located in the upwelling region ([Fig. 2](#)). Model-group 3 seems to group models
369 characterized by an equatorward shift of the main structures, since the region-cluster 1 of tropical
370 waters is not reproduced and Region-clusters 4 and 5 of extratropical waters are overestimated.
371 [Fig. 4](#) indeed shows that this Model-group is very close to the Regions-clusters 4 and 5, which
372 correspond to the extratropical and the transition geographical regions. Model-group 2
373 misrepresents the region of the Canary upwelling. Model-group 1 overestimates the SST seasonal
374 cycle in all the tropical open Atlantic. These two last model-groups overestimate the region-
375 Cluster 1, again consistently with their position in [Fig. 4](#). A detailed physical interpretation of the
376 Model-groups is nevertheless beyond the scope of this paper. Clearly Model-All represents the
377 SST seasonal cycle of the off-shore ocean, but it proposes a very poor representation of the
378 upwelling region.

379 Two models (models 7 and 25) have a better skill than Model-group 4 and Model-All.
380 These two models are very close to the observations on the first two axes of the MCA ([Fig 4](#)). It
381 is easily seen that Model-group 4 and the projection of Model-All on this plane is farther than
382 that of model 7 and model 25 from the observation projection. This explains the lower
383 performance of these two multi-models as compared to models 7 and 25. In the present case, the
384 method permits to determine the best models (model 7 and model 25) and to outline the best

385 multi-model (Model-group 4) whose skill is better than any model with a probability of 95%
386 (number of models whose skill is smaller than the skill of Model-group 4 with respect to the total
387 number of models). Projection of the models on the other planes of the MCA analysis should
388 confirm this interpretation. One could then question the use of Model-group 4 rather than model
389 7 or model 25 individually. Furthermore, we argue that multi-model averages are in general more
390 robust for climate studies than the use of a single model that can have good performance for a
391 very specific set of constraints but not for neighboring ones. The following section will partly
392 justify this point.

393

394 **5 - Analysis of the climate models over a zoomed upwelling region**

395 The classification presented above relies largely on the ability of the models to represent
396 the offshore seasonal cycle of the SST. In the following, we propose to test the classification over
397 a much more reduced area in order to focus the analysis on the upwelling area. This “zoomed
398 upwelling region” is shown in [Fig. 1](#).

399 As for the extended region, we partitioned the observations of the zoomed upwelling
400 region with a SOM (ZSOM in the following) followed by a HAC. We then applied a new MCA
401 to regroup the climate models. We did a similar analysis as this performed in section 4. We
402 obtained four new well separated region-clusters denoted ZRegion-clusters. [Fig. 7](#) shows the four
403 ZRegion-clusters obtained from ERSSTv3b observations together with their associated mean
404 SST seasonal cycle. Again, the ZRegion-clusters are spatially coherent. The upwelling area is
405 now decomposed into three ZRegion-clusters (ZRegion-clusters 2, 3, 4). This new decomposition
406 thus refines the study performed for the extended region: ZRegion-cluster 1 represents the
407 offshore ocean, its grid points typically have a SST seasonal cycle amplitude of 4°C, very similar
408 to Region-cluster 4 in the classification performed over the extended region ([Fig. 2](#)). ZRegion-
409 cluster-4 identifies the core of the Senegalo-Mauritanian region, with grid points characterized by
410 the greatest amplitude of the SST seasonal cycle of the domain, typically 6.5°C. It is interesting
411 to note that an additional upwelling ZRegion-cluster (ZRegion-cluster 3) appears south of
412 ZRegion-cluster 4. Indeed, several studies have shown that the Cape Verde peninsula, located
413 around 15°N, separates the upwelling region into two distinct areas having a different behavior
414 north and south of this peninsula (Sirven et al., 2019; Sylla et al., 2019). The location of the

415 separation between ZRegion-cluster 3 and 4 is determined with some uncertainty due to the
416 coarse resolution (1°) of the ocean models. ZRegion-cluster 3 is marked by a time shift of the
417 seasonal cycle: the warmest season seems to occur somewhat one month earlier than in the other
418 regions as clearly seen in [Fig. 7](#) (left panel, yellow curve in June). Due a classification using a
419 much larger region, such a characteristic does not appear in the extended area study. The physical
420 interpretation of the SST seasonal cycle of this ZRegion-cluster is beyond the scope of the
421 present study, but one can suspect a role of the ITCZ seasonal migration covering these grid
422 points earlier than further north. Finally, ZRegion-cluster 2 is a transition between the large scale
423 ocean and the upwelling region.

424 As for the extended region, we applied a MCA analysis to the (47×4) matrix $R = [R_{mi}]$
425 whose elements represent the skills of the four clusters (i) of the 47 models. This MCA was
426 followed by a HAC leading the definition of five ZModel-groups. The members of each group
427 are given in appendix. [Fig. 8](#) shows the ZRegion-cluster obtained in the zoomed area by
428 projecting these five ZModel-groups and Model-All model on the ZSOM and their associated
429 performances. ZModel-group 1 is the worst performing one: only 25% of the grid cells fall in the
430 same class as for the observations. The structure of this model-group shows that it is
431 characterized by an homogeneous amplitude of the seasonal cycle over the whole domain,
432 suggesting a largely reduced upwelling: only one grid point at the coast has an enhanced SST
433 seasonal cycle as compared to the large scale tropical ocean. ZModel-group 2 is the best
434 performing one: 66% of the grid points are assigned to the correct class and the general picture
435 indeed represents a four-class picture fairly consistent with the observed structure ([Fig. 7](#)).
436 Important biases yet remain. In particular, the ZRegion-clusters 2 and 4 characterizing the
437 upwelling extend too far offshore. The three other ZModel-groups are intermediate. A relatively
438 reduced upwelling area, with an underestimated SST seasonal cycle, characterizes ZModel-
439 groups 3 and 4. ZModel-group 5 corresponds to a shift of the upwelling region towards the north.
440 Model-All also shows a strongly reduced seasonal cycle, with a large number of pixels in the
441 intermediate ZRegion-cluster 3 and very few in the ZRegion-cluster 4. The ZRegion-cluster 3,
442 representing the southern part of the Senegalo-Mauritanian upwelling, does not appear in the
443 pattern of Model-All.

444 It is notable that all the models forming ZModel-group 2 are included in Model-group 4.
445 For a more precise assessment, we can also project the entire Model-group 4, identified as the
446 best multi-model ensemble over the extended region, on the ZSOM (Fig. 9, right). We notice that
447 the performance of Model-group 4 remains high on this projection, indicating some robustness of
448 this multi-model ensemble. Moreover, this ensemble now outperforms the single best model
449 identified over the extended region (Fig. 9, left panel). This result gives further confidence in the
450 use of multi-model averages, illustrating that one single model can be very skillful over a specific
451 region, or for a specific analysis, but multi-model averages are more robust across various
452 analysis and/or regions.

453 **6 – Impact of climate change on the Senegalo-Mauritanian upwelling**

454 **6.1 Representation of the upwelling in the CMIP5 climate models clusters**

455 In this section, we compare the representation of the Senegalo-Mauritanian upwelling system
456 given by the two best Model-groups identified above (Model-group 4 and ZModel-group 2). For
457 this evaluation, we use two of the five indices used by (Sylla et al., 2019) to evaluate the full
458 database, namely the intensity of the SST seasonal cycle and the offshore Ekman transport at the
459 coast. The former is specific to the seasonal variability of the Senegalo-Mauritanian upwelling
460 system, and it has been used for the classification. The latter is more general and although it has
461 recently been shown to partly represent the volume of the upwelled waters (Jacox et al., 2018), it
462 is extensively used in the scientific literature to characterize upwelling regions (Cropper et al.,
463 2014; Rykaczewski et al., 2015; Wang et al., 2015). Note also that following Sylla et al., 2019,
464 evaluation is performed on the period [1985-2005]. This period slightly differs from the
465 classification period but the SST seasonal cycle is not significantly different (not shown).

466 Fig. 10 compares the amplitude of the SST seasonal cycle as represented in the
467 observations, Model-All, Model-group 4 and ZModel-group 2 identified above. Consistently with
468 Fig. 6 and 8, Model-All dramatically underestimates the upwelling signature in terms of SST
469 seasonal cycle as compared to the observations. Model-group 4 and ZModel-group 2 yield
470 improved results: the area of enhanced SST seasonal cycle is larger both in latitude and
471 longitude, with stronger SST amplitude values. This confirms the efficiency of the selection
472 operated above. Nevertheless, ZModel-group 2 yields a realistic SST amplitude pattern along the
473 coast but it extends too far offshore. Furthermore, in ZModel-group 2, the subtropical area (in

474 green in Fig 10) extends too far towards the south, in particular in the western part of the basin.
475 The tropical area, characterized by limited amplitude of the seasonal cycle of SST (deep blue in
476 Fig. 10), is shifted to the south as compared to the observations. In other words, the large scale
477 thermal - and thus probably dynamical - structure of the region is poorly represented in ZModel-
478 group 2. Finally, Model-group 4 is the least biased one.

479 The intensity of the wind stress parallel to the coast, inducing offshore Ekman transport
480 and consequently an Ekman pumping at the coast, is generally considered as the main driver of
481 the upwelling. We therefore also tested the representation of this driver in the different Model-
482 groups. The idea is to evaluate the impact of the model selection performed above on the
483 representation of an independent variable by the Model-groups. Fig. 11 shows the latitude-time
484 evolution of the meridional oceanic wind stress, considering that the coast in the studied region is
485 oriented approximately meridionally, so that the offshore Ekman transport is mainly zonal. Note
486 that in Fig. 11, southward winds have positive values so that they correspond to a westward
487 Ekman transport, favorable to upwelling. Panel (a) shows that the observed meridional wind
488 stress is, all year long, favorable to the upwelling north of 20°N. At these latitudes, the
489 meridional wind stress is stronger in summer. Conversely, between 12°N and 20°N, in the
490 latitude band of the Senegalo-Mauritanian upwelling, the wind blows southward with a very
491 weak intensity in summer and it even changes direction in the southern part of this latitude band.
492 It is favorable to the upwelling in winter-spring, which explains why the Senegalo-Mauritanian
493 upwelling occurs during this season with a maximum of intensity in March-April (Capet et al.,
494 2017; Farikou et al., 2015). The main bias of Model-All (Fig. 11b) is due to the fact that the
495 wind stress never reverses between 12°N and 20°N. It weakens in the southern part of the
496 Senegalo-Mauritanian latitude band, i.e. south of the Cape Verde peninsula (15°N), but does not
497 become negative. North of the Cape Verde peninsula, it also blows from the north in summer, so
498 that the Senegalo-Mauritanian upwelling lacks seasonality. This bias is corrected in Model-group
499 4 and ZModel-group 2 (Fig. 11, panels c and d) that are, in this aspect, more realistic than Model-
500 All. Model-group 4 shows a slight extension of the time and latitude range where the oceanic
501 wind stress reverses sign. This constitutes an improvement. The southward wind is nevertheless
502 too strong in winter on the [12°N-20°N] latitude band as well as further south from December to
503 March. These two remaining biases are further reduced in ZModel-group 2. This latter model
504 yields the most realistic seasonal cycle of meridional oceanic wind stress on the latitude band

505 under study. This is consistent with a very localized model selection, as the wind index is itself
506 localized along the coast.

507 To conclude, Model-group 4 and ZModel-group 2 perform in general better than Model-All in
508 reproducing the major, characteristic features of the Senegalo-Mauritanian upwelling. This result
509 confirms the relevance of the multi-model selection we have presented above. Applying the
510 methodology over a relatively large region allows better constraining the spatial extent and
511 pattern of the SST signature of the upwelling than the reduced area. The latter however yields a
512 better representation of the wind seasonality along the coast.

513 **6.2 Response of the Senegalo-Mauritanian upwelling to global warming.**

514 In this section, we examine the response of the upwelling system given by the different
515 multi-model groups we selected to global warming. For this, we compared the two indices
516 analyzed above in present-day and future conditions. The present-day conditions are taken as
517 above as the climatological average of historical simulations over the period [1985-2005]. The
518 future period is taken as the climatological average of the RCP8.5 scenario over the period [2080-
519 2100]. [Fig. 12](#) shows the difference of the SST seasonal cycle amplitude between these two
520 periods. The general behavior is that the SST cycle amplitude will reduce in the upwelling region.
521 Sylla et al., 2019 showed that this is primarily due to a warming of the winter temperature, thus
522 suggesting that the upwelling signature at the surface will reduce. On the other hand, this figure
523 shows that the upwelling signature will increase along the Canary current, which flows along the
524 coast of Morocco, as well as in the subtropical part of our domain. This behavior is observed in
525 the three multi-model ensembles. Yet, the two selected Model-groups suggest a weaker decrease
526 of the SST seasonal cycle in the upwelling region than the one given by Model-All. ZModel-
527 group 2 shows an even weaker decrease mainly confined in the southern part of the upwelling
528 region. This result echoes findings of Sylla et al., 2019 based on another indicator of the
529 upwelling imprint on the SST: they showed that the difference between the SST at the coast and
530 offshore is expected to decrease more in the southern part of the Senegalo-Mauritanian upwelling
531 system (SMUS) than in the north . We hypothesize that the study conducted on the reduced area
532 permits separation of the Senegalo-Mauritanian upwelling system into two clusters, a northern
533 one (ZRegion 4) and a southern one (ZRegion-3) ([Fig. 8](#)) which enables to distinguish this
534 specific response.

535 The meridional wind stress also generally weakens under climate change in the [12°N-
536 20°N] latitude band (Fig. 13), suggesting a general reduction of the upwelling intensity. From
537 December to March, this is particularly true in the southernmost region of the Senegalo-
538 Mauritanian band, consistent with the results of (Sylla et al., 2019). The wind pattern inferred
539 from the two Model-groups (Fig. 13, middle and right panels) present a higher seasonal
540 variability than those of Model-All (left panel). The winter reduction of the southward wind
541 stress is slightly more confined to the southern region in ZModel-group 2, especially at the end of
542 the upwelling season (March-April) when the upwelling intensity is the strongest. This may be
543 consistent with the reduced seasonal cycle in the southernmost part of the upwelling identified
544 above.

545 **7 - Discussion and Conclusion**

546 This paper proposed a novel methodology for selecting efficient climate models on a specific
547 area with respect to observations and according to well-defined statistical criteria. The present
548 study has specifically focused on the ability of climate models to reproduce the ocean SST annual
549 cycle observed in specific sub-regions of the studied domain during the period 1975-2005 as
550 reported in the ERSST_v3b data set. These sub-regions were defined by a neural classifier
551 (SOM) as clusters having similar seasonal SST cycle anomalies with respect to some statistical
552 characteristics, and were therefore named region-clusters. They correspond to ocean areas having
553 well marked oceanographic specificities.

554 We then checked the ability of the different climate models to reproduce the region-clusters
555 defined on the observation dataset with a SOM. The better a climate model fits the clusters
556 computed with the SST observation, the higher the skill of the model. To evaluate this, we
557 defined geographical regions in the different CMIP5 climate models by projecting the SST
558 annual cycle anomalies of each model grid point onto the SOM. Each grid point is associated
559 with a cluster on the SOM map and consequently to a region-cluster on the geographical map.
560 We built a similarity criterion by counting the number of grid points in a region-cluster of a
561 given model matching the same region cluster defined by processing the observation field.
562 We then computed the ratio between that matching number and the number of pixels of the
563 region-cluster of the model under study. We estimated the total skill of a model by averaging
564 the 7 ratios associated with the 7 region clusters. Note that this procedure presents the advantage

565 of giving the same weight to each region-cluster whatever its number of grid points and its
566 proximity with the upwelling region. This procedure respects the clustering done by the SOM
567 since the different clusters have an equal weight in the skill computation. In its present definition,
568 the total skill is a number between 0 and 1, the higher the skill, the better the fit. Other measures
569 of the total skill of a Model-group could nevertheless be defined depending on the objective of
570 the study. One may compare the skill of individual models over a specific region-cluster of
571 interest, or analyze the pattern of skill in one specific model and its sensitivity to possible various
572 parameterization schemes. The extraction of information embedded in the vector-skill whose 7
573 components are the skills associated with the 7 sub-regions and the resulting efficient multi-
574 model combination imply the use of advanced statistical tools such as the MCA. Moreover the
575 vector skill also contains information behavior of models in terms of large offshore ocean
576 circulation as well as in the upwelling region. It could thus be used to diagnose the deficiencies of
577 some climate models with respect to the modeling of physical processes. Another contribution of
578 the MCA is the visualization of the 47 models and the observations on the plane constituted by
579 the first two MCA axes, which represents 70% of the information embedded in the data. The
580 similarities of the climate models with respect to the observations and the region-clusters can be
581 clearly visualized. The ‘mean’ skill associated with each climate model and proposed in this
582 study is easy to use but is far less informative than the vector-skill whose 7 components are the
583 skills associated with the 7 sub-regions.

584 Such a multi-model ensemble selection allows sampling a set of models in order to obtain a more
585 realistic climatology over the region of interest. The response of the upwelling to climate change
586 given by the different multi-model ensembles is quite robust in the sense that they give similar
587 qualitative answers. However, a too-selective ensemble of models may lead to noisy patterns. A
588 compromise thus has to be found: a large number of models leads to smoothed biases and
589 unrealistic patterns, but also damps the characteristics of the selection. On the other hand,
590 selecting the most realistic models may yield spurious biases in the ensemble mean.

591 As discussed in the introduction, different criteria have been used for extracting some efficient
592 models from the CMIP5 models used for climatic studies. The most common parameter is the
593 average annual surface mean temperature of the grid points of the region under study.
594 However,(Knutti et al., 2006) used the seasonal cycle in surface temperature, represented by the

595 seasonal amplitude calculated as summer June–August (JJA) minus winter December–February
596 (DJF) temperatures. This criterion is more informative than the annual mean temperature since
597 the amplitude of the seasonal variability is an important criterion characterizing the validity of a
598 climate model. In the present work, we used a more informative criterion which is formed of the
599 monthly temperature cycle anomaly represented by a 12-component vector, each component
600 representing the average monthly temperature of the year we consider. This new criterion allows
601 account to be taken of the amplitude and phase of seasonal variability while the Knutti et al.,
602 2006 criterion only takes into account the amplitude of the seasonal variability. Note however
603 that it implies a good geophysical knowledge of the region under interest, in order to determine
604 the relevant region-clusters after the SOM. It is also very specific to the Senegal-Mauritania
605 upwelling region. Furthermore, Sylla et al., 2019 extensively discussed the possible differences
606 among several indices aiming at characterizing the upwelling and the need to use some of them to
607 have a complete understanding of this coastal phenomenon. This conclusion is probably general
608 to any physical process of the climate system. In the present study, the model selection is based
609 on only one signature of the SMUS. Several possibilities can be envisaged to improve the
610 resolution of this problem such as merging several indices like SST, temperature at several
611 depths, wind vector or ocean currents. This approach could also allow a selection of models
612 based on the representation of several distinct regional behaviors. In spite of several subjective
613 choices, including the studied domain and the statistical metrics, we argue that this method is a
614 step towards an objective selection of models, based on a quantitative assessment rather than a
615 qualitative analysis of maps of performance.

616 The methodology is general and can be adapted to any climate or oceanographic phenomenon.
617 Different applications of the multi-model selection strategy proposed in the present study can
618 also be envisaged. Firstly, from a purely modeling point of view, the projection of the models on
619 the SOM (or ZSOM) and the results of the HAC yield a very enlightening description of a given
620 model behavior in terms of region-clusters of the area under study. Such a procedure could
621 advantageously be used by individual modeling groups to identify, analyze and therefore
622 hopefully reduce their model biases in a targeted region. Secondly, from a physical point of view,
623 an identified Model-group can be used to analyze the targeted region (here the SMUS) in terms
624 of processes, with the advantages of a subset of models which have been selected from
625 quantitative criteria. Such an application has been briefly illustrated by showing how the selected

626 Model-group represents an important additional characteristic of the SMUS, not used for the
627 selection, namely Ekman pumping. A promising reduction of biases of the full multi-model mean
628 ensemble has been identified, opening possibilities for process studies based on this sub-
629 ensemble of the CMIP5 database. A third application of the selection lies in the prediction of the
630 future climate. Here, we have shown that selected multi-model ensembles may provide a more
631 precise description of the future behavior of the SMUS. It may nevertheless be important to note
632 that these conclusions are based on the assumption that the CMIP5 models, which have been
633 selected according to their present-day characteristics, are the most reliable in terms of future
634 projections, which can be questioned and refined (Lutz et al., 2016; Reifen and Toumi, 2009).

635 As discussed in the introduction, the concept of “model democracy”, suggesting that all models
636 should be equally considered in multi-model ensemble is now strongly questioned (Knutti et al.,
637 2017). The present study proposes a promising way to improve the quality of multi-model
638 ensemble in terms of model selection. Deep advances in the field of multi-model analysis and
639 selection can be expected from the emerging topic of climate informatics (Monteleoni et al.,
640 2016) as it has been shown through the present study. Machine learning can indeed provide
641 efficient tools to make the best out of the extraordinary but imperfect tools that are the climate
642 models and multi-model intercomparison efforts.

643

644 **Acknowledgments**

645 NOAA_ERSST_V3b data provided by the NOAA/OAR/ESRL PSD, Boulder, Colorado, USA,
646 from their Web site at <https://www.esrl.noaa.gov/psd/> The research leading to these results has
647 received funding from the NERC/DFID Future Climate for Africa program under the SCUS-2050
648 project, emanating from AMMA-2050 project, grant number NE/M019969/1. The authors also
649 acknowledge support from the Laboratoire Mixte International ECLAIRS2, supported by the
650 french Institut de Recherche pour le Développement. J.M. was also supported by the H2020-
651 EUCP project under grant agreement 776613. To analyze the CMIP5 data, this study benefited
652 from the IPSL Prodiguer-Ciclad facility which is supported by CNRS, UPMC, Labex L-IPSL
653 which is funded by the ANR (Grant #ANR-10-LABX-0018) and by the European FP7 IS-ENES2
654 project (Grant #312979). The author gratefully thank Matthew Menary for a careful reading of
655 the manuscript.

656 **Code and Data availability:** The model output used for this study is freely available on the
657 ESGF database for example following this url: <https://esgf-node.ipsl.upmc.fr/search/cmip5-ipsl/>.
658 The SST data were downloaded from

659 <https://www.esrl.noaa.gov/psd/data/gridded/data.noaa.ersst.v3.html> and the winds data
660 here: <https://podaac.jpl.nasa.gov> . The code developed for the core computations of this study can
661 be found under: 10.5281/zenodo.3476724. This code allows reproducing Fig. 2, 3, 6, 7 and 8.

662 **Author contribution:** JM initially proposed the idea, ST and MC translated it in terms of
663 methodology and coordinated the method development, CS and CM developed the code and
664 produced the figures, CS, CM, MC, ST all contributed to the statistical analysis. As provided the
665 initial definition of the upwelling index and performed the analysis under climate change that is
666 presented in section 6. JM, MC and ST prepared the manuscript with contributions from all the
667 authors.

668 **Références**

669 Borodina, A., Fischer, E. M. and Knutti, R.: Potential to constrain projections of hot temperature
670 extremes, *J. Clim.*, 30(24), 9949–9964, doi:10.1175/JCLI-D-16-0848.1, 2017.

671 Capet, X., Estrade, P., Machu, E., Ndoye, S., Grelet, J., Lazar, A., Marié, L., Dausse, D.,
672 Brehmer, P., Capet, X., Estrade, P., Machu, E., Ndoye, S., Grelet, J., Lazar, A., Marié, L.,
673 Dausse, D. and Brehmer, P.: On the Dynamics of the Southern Senegal Upwelling Center:
674 Observed Variability from Synoptic to Superinertial Scales, *J. Phys. Oceanogr.*, 47(1), 155–180,
675 doi:10.1175/JPO-D-15-0247.1, 2017.

676 Collins, M., Knutti, R., Dufresne, J.-L., Fichet, T., Friedlingstein, P., Gao, X., Gutowski, W. J.,
677 Johns, T., Krinner, G., Shongwe, M., Tebaldi, C., Weaver, A. J. and Wehner, M.: Long-term
678 Climate Change: Projections, Commitments and Irreversibility, in *Climate Change 2013: The*
679 *Physical Science Basis. Contribution of Working Group I to the Fifth Assessment Report of the*
680 *Intergovernmental Panel on Climate Change*, edited by T. F. Stocker, G.-K. D. Qin, M. Plattner,
681 S. K. Tignor, J. Allen, A. Boschung, Y. Nauels, Y. Xia, P. M. Bex, and V. Midgley, Cambridge
682 University Press, Cambridge, United Kingdom and New York, NY, USA., 2014.

683 Cox, P. M., Pearson, D., Booth, B. B., Friedlingstein, P., Huntingford, C., Jones, C. D. and Luke,
684 C. M.: Sensitivity of tropical carbon to climate change constrained by carbon dioxide variability,
685 *Nature*, 494(7437), 341–344, doi:10.1038/nature11882, 2013.

686 Cropper, T. E., Hanna, E. and Bigg, G. R.: Spatial and temporal seasonal trends in coastal
687 upwelling off Northwest Africa, 1981-2012, *Deep. Res. Part I Oceanogr. Res. Pap.*, 86, 94–111,
688 doi:10.1016/j.dsr.2014.01.007, 2014.

689 Deangelis, A. M., Qu, X., Zelinka, M. D. and Hall, A.: An observational radiative constraint on
690 hydrologic cycle intensification, *Nature*, 528(7581), 249–253, doi:10.1038/nature15770, 2015.

691 Demarcq, H. and Faure, V.: Coastal upwelling and associated retention indices derived from
692 satellite SST. Application to Octopus vulgaris recruitment, *Oceanol. Acta*, 23(4), 391–408,
693 doi:10.1016/S0399-1784(00)01113-0, 2000.

694 Farikou, O., Sawadogo, S., Niang, A., Diouf, D., Brajard, J., Mejia, C., Dandonneau, Y., Gasc,
695 G., Crepon, M. and Thiria, S.: Inferring the seasonal evolution of phytoplankton groups in the
696 Senegalo-Mauritanian upwelling region from satellite ocean-color spectral measurements, *J.*
697 *Geophys. Res. Ocean.*, 120(9), 6581–6601, doi:10.1002/2015JC010738, 2015.

- 698 Fasullo, J. T. and Trenberth, K. E.: A less cloudy future: The role of subtropical subsidence in
699 climate sensitivity, *Science* (80-.), 338(6108), 792–794, doi:10.1126/science.1227465, 2012.
- 700 Faye, S., Lazar, A., Sow, B. A. and Gaye, A. T.: A model study of the seasonality of sea surface
701 temperature and circulation in the Atlantic North-eastern Tropical Upwelling System, *Front.*
702 *Phys.*, 3(September), 1–20, doi:10.3389/fphy.2015.00076, 2015.
- 703 Gao, Y., Lu, J. and Leung, L. R.: Uncertainties in projecting future changes in atmospheric rivers
704 and their impacts on heavy precipitation over Europe, *J. Clim.*, 29(18), 6711–6726,
705 doi:10.1175/JCLI-D-16-0088.1, 2016.
- 706 Gordon, N. D., Jonko, A. K., Forster, P. M. and Shell, K. M.: An observationally based constraint
707 on the water-vapor feedback, *J. Geophys. Res. Atmos.*, 118(22), 12435–12443,
708 doi:10.1002/2013JD020184, 2013.
- 709 Hewitson, B. C. and Crane, R. G.: Self-organizing maps: Applications to synoptic climatology,
710 *Clim. Res.*, 22(1), 13–26, doi:10.3354/cr022013, 2002.
- 711 Huber, M. and Knutti, R.: Anthropogenic and natural warming inferred from changes in Earth’s
712 energy balance, *Nat. Geosci.*, 5(1), 31–36, doi:10.1038/ngeo1327, 2012.
- 713 Jacox, M. G., Edwards, C. A., Hazen, E. L. and Bograd, S. J.: Coastal Upwelling Revisited:
714 Ekman, Bakun, and Improved Upwelling Indices for the U.S. West Coast, *J. Geophys. Res.*
715 *Ocean.*, 1–19, doi:10.1029/2018JC014187, 2018.
- 716 Jain, A. K. and Dubes, R. C.: Algorithms for clustering data, Prentice Hall, Inc., Englewood.
717 Cliffs., 1988.
- 718 Jouini, M., Lévy, M., Crépon, M. and Thiria, S.: Reconstruction of satellite chlorophyll images
719 under heavy cloud coverage using a neural classification method, *Remote Sens. Environ.*, 131,
720 232–246, doi:10.1016/j.rse.2012.11.025, 2013.
- 721 Jouini, M., Béranger, K., Arsouze, T., Beuvier, J., Thiria, S., Crépon, M. and Taupier-Letage, I.:
722 The Sicily Channel surface circulation revisited using a neural clustering analysis of a high-
723 resolution simulation, *J. Geophys. Res. Ocean.*, 121(7), 4545–4567, doi:10.1002/2015JC011472,
724 2016.
- 725 Knutti, R., Meehl, G. A., Allen, M. R. and Stainforth, D. A.: Constraining climate sensitivity
726 from the seasonal cycle in surface temperature, *J. Clim.*, 19(17), 4224–4233,
727 doi:10.1175/JCLI3865.1, 2006.
- 728 Knutti, R., Furrer, R., Tebaldi, C., Cermak, J., Meehl, G. A., Knutti, R., Furrer, R., Tebaldi, C.,
729 Cermak, J. and Meehl, G. A.: Challenges in Combining Projections from Multiple Climate
730 Models, *J. Clim.*, 23(10), 2739–2758, doi:10.1175/2009JCLI3361.1, 2010.
- 731 Knutti, R., Sedláček, J., Sanderson, B. M., Lorenz, R., Fischer, E. M. and Eyring, V.: A climate
732 model projection weighting scheme accounting for performance and interdependence, *Geophys.*
733 *Res. Lett.*, 44(4), 1909–1918, doi:10.1002/2016GL072012, 2017.
- 734 Kohonen, T.: Essentials of the self-organizing map, *Neural Networks*, 37, 52–65,
735 doi:10.1016/j.neunet.2012.09.018, 2013.
- 736 Kounta, L., Capet, X., Jouanno, J., Kolodziejczyk, N., Sow, B. and Gaye, A. T.: A model

- 737 perspective on the dynamics of the shadow zone of the eastern tropical North Atlantic – Part 1:
738 the poleward slope currents along West Africa, *Ocean Sci.*, 14(5), 971–997, doi:10.5194/os-14-
739 971-2018, 2018.
- 740 Lambert, S. M. and Boer, G. J.: CMIP1 evaluation and intercomparison of coupled climate
741 models, *Clim. Dyn.*, 17, 83–106, doi:10.1007/pl00013736, 2001.
- 742 Liu, Y., Weisberg, R. H. and Mooers, C. N. K.: Performance evaluation of the self-organizing
743 map for feature extraction, *J. Geophys. Res. Ocean.*, 111(5), C05018,
744 doi:10.1029/2005JC003117, 2006.
- 745 Loeb, N. G., Wang, H., Cheng, A., Kato, S., Fasullo, J. T., Xu, K.-M. and Allan, R. P.:
746 Observational constraints on atmospheric and oceanic cross-equatorial heat transports: revisiting
747 the precipitation asymmetry problem in climate models, *Clim. Dyn.*, 46(9–10), 3239–3257,
748 doi:10.1007/s00382-015-2766-z, 2015.
- 749 Lutz, A. F., ter Maat, H. W., Biemans, H., Shrestha, A. B., Wester, P. and Immerzeel, W. W.:
750 Selecting representative climate models for climate change impact studies: an advanced
751 envelope-based selection approach, *Int. J. Climatol.*, 36(12), 3988–4005, doi:10.1002/joc.4608,
752 2016.
- 753 Masson, D. and Knutti, R.: Climate model genealogy, *Geophys. Res. Lett.*, 38(8),
754 doi:10.1029/2011GL046864, 2011.
- 755 Monteleoni, C., Schmidt, G. A., Alexander, F., Niculescu-Mizil, A., Steinhäuser, K., Tippett,
756 M., Banerjee, A., Benno Blumenthal, M., Ganguly, A. R., Smerdon, J. E. and Tedesco, M.:
757 Climate informatics, in *Computational Intelligent Data Analysis for Sustainable Development*,
758 pp. 81–126, NASA., 2016.
- 759 Ndoye, S., Capet, X., Estrade, P., Sow, B. A., Dagonne, D., Lazar, A., Gaye, A. T. and Brehmer,
760 P.: SST patterns and dynamics of the southern Senegal-Gambia upwelling center, *J. Geophys.*
761 *Res. Ocean.*, 119(12), 8315–8335, doi:10.1002/2014JC010242, 2014.
- 762 Niang, A., Gross, L., Thiria, S., Badran, F. and Moulin, C.: Automatic neural classification of
763 ocean colour reflectance spectra at the top of the atmosphere with introduction of expert
764 knowledge, *Remote Sens. Environ.*, 86(2), 257–271, doi:10.1016/S0034-4257(03)00113-5, 2003.
- 765 Niang, A., Badran, F., Moulin, C., Crépon, M. and Thiria, S.: Retrieval of aerosol type and
766 optical thickness over the Mediterranean from SeaWiFS images using an automatic neural
767 classification method, *Remote Sens. Environ.*, 100(1), 82–94, doi:10.1016/j.rse.2005.10.005,
768 2006.
- 769 O’Gorman, P. A., Allan, R. P., Byrne, M. P. and Previdi, M.: Energetic Constraints on
770 Precipitation Under Climate Change, *Surv. Geophys.*, 33(3–4), 585–608, doi:10.1007/s10712-
771 011-9159-6, 2012.
- 772 Phillips, T. J. and Gleckler, P. J.: Evaluation of continental precipitation in 20th century climate
773 simulations: The utility of multimodel statistics, *Water Resour. Res.*, 42(3),
774 doi:10.1029/2005WR004313, 2006.
- 775 Praveen Kumar, B., Vialard, J., Lengaigne, M., Murty, V. S. N. and McPhaden, M. J.: TropFlux:
776 air-sea fluxes for the global tropical oceans—description and evaluation, *Clim. Dyn.*, 38(7–8),

- 777 1521–1543, doi:10.1007/s00382-011-1115-0, 2011.
- 778 Rayner, N. A.: Global analyses of sea surface temperature, sea ice, and night marine air
779 temperature since the late nineteenth century, *J. Geophys. Res.*, 108(D14), 4407,
780 doi:10.1029/2002JD002670, 2003.
- 781 Reichler, T. and Kim, J.: How well do coupled models simulate today's climate?, *Bull. Am.*
782 *Meteorol. Soc.*, 89(3), 303–311, doi:10.1175/BAMS-89-3-303, 2008.
- 783 Reifen, C. and Toumi, R.: Climate projections: Past performance no guarantee of future skill?,
784 *Geophys. Res. Lett.*, 36(13), 1–5, doi:10.1029/2009GL038082, 2009.
- 785 Reusch, D. B., Alley, R. B. and Hewitson, B. C.: North Atlantic climate variability from a self-
786 organizing map perspective, *J. Geophys. Res. Atmos.*, 112(2), D02104,
787 doi:10.1029/2006JD007460, 2007.
- 788 Richardson, A. J., Risi En, C. and Shillington, F. A.: Using self-organizing maps to identify
789 patterns in satellite imagery, *Prog. Oceanogr.*, 59(2–3), 223–239,
790 doi:10.1016/j.pocean.2003.07.006, 2003.
- 791 Rykaczewski, R. R., Dunne, J. P., Sydeman, W. J., García-Reyes, M., Black, B. A. and Bograd,
792 S. J.: Poleward displacement of coastal upwelling-favorable winds in the ocean's eastern
793 boundary currents through the 21st century, *Geophys. Res. Lett.*, 42(15), 6424–6431,
794 doi:10.1002/2015GL064694, 2015.
- 795 Santer, B. D., Taylor, K. E., Gleckler, P. J., Bonfils, C., Barnett, T. P., Pierce, D. W., Wigley, T.
796 M. L., Mears, C., Wentz, F. J., Bruggemann, W., Gillett, N. P., Klein, S. A., Solomon, S., Stott,
797 P. A. and Wehner, M. F.: Incorporating model quality information in climate change detection
798 and attribution studies, *Proc. Natl. Acad. Sci.*, 106(35), 14778–14783,
799 doi:10.1073/pnas.0901736106, 2009.
- 800 Sawadogo, S., Brajard, J., Niang, A., Lathuiliere, C., Crépon, M. and Thiria, S.: Analysis of the
801 Senegalo-Mauritanian upwelling by processing satellite remote sensing observations with
802 topological maps., in *Proceedings of the International Joint Conference on Neural Networks*, pp.
803 2826–2832, IEEE., 2009.
- 804 Sirven, J., Mignot, J. and Crépon, M.: Generation of Rossby waves off the Cape Verde Peninsula:
805 The role of the coastline, *Ocean Sci.*, 15(6), 1667–1690, doi:10.5194/os-15-1667-2019, 2019.
- 806 Smith, T. M., Reynolds, R. W., Peterson, T. C. and Lawrimore, J.: Improvements to NOAA's
807 historical merged land-ocean surface temperature analysis (1880–2006), *J. Clim.*, 21(10), 2283–
808 2296, doi:10.1175/2007JCLI2100.1, 2008.
- 809 Son, S. W., Gerber, E. P., Perlwitz, J., Polvani, L. M., Gillett, N. P., Seo, K. H., Eyring, V.,
810 Shepherd, T. G., Waugh, D., Akiyoshi, H., Austin, J., Baumgaertner, A., Bekki, S., Braesicke, P.,
811 Brühl, C., Butchart, N., Chipperfield, M. P., Cugnet, D., Dameris, M., Dhomse, S., Frith, S.,
812 Garny, H., Garcia, R., Hardiman, S. C., Jöckel, P., Lamarque, J. F., Mancini, E., Marchand, M.,
813 Michou, M., Nakamura, T., Morgenstern, O., Pitari, G., Plummer, D. A., Pyle, J., Rozanov, E.,
814 Scinocca, J. F., Shibata, K., Smale, D., Teyssdre, H., Tian, W. and Yamashita, Y.: Impact of
815 stratospheric ozone on Southern Hemisphere circulation change: A multimodel assessment, *J.*
816 *Geophys. Res. Atmos.*, 115(19), D00M07, doi:10.1029/2010JD014271, 2010.

- 817 Stegehuis, A. I., Vautard, R., Ciais, P., Teuling, A. J., Jung, M. and Yiou, P.: Summer
818 temperatures in Europe and land heat fluxes in observation-based data and regional climate
819 model simulations, *Clim. Dyn.*, 41(2), 455–477, doi:10.1007/s00382-012-1559-x, 2013.
- 820 Stocker, T. F., Qin, D., Plattner, G.-K., Tignor, M., Allen, S. K., Boschung, J., Nauels, A., Xia,
821 Y., Bex, V. and Midgley, P. M., Eds.: *Climate Change 2013: The Physical Science Basis.*
822 *Contribution of Working Group I to the Fifth Assessment Report of the Intergovernmental Panel*
823 *on Climate Change*, Cambridge University Press, United Kingdom and New York, NY, USA.,
824 2013.
- 825 Sylla, A., Mignot, J., Capet, X. and Gaye, A. T.: Weakening of the Senegalo–Mauritanian
826 upwelling system under climate change, *Clim. Dyn.*, 53(7), 4447–4473, doi:10.1007/s00382-019-
827 04797-y, 2019.
- 828 Tan, I., Storelvmo, T. and Zelinka, M. D.: Observational constraints on mixed-phase clouds
829 imply higher climate sensitivity, *Science (80-.)*, 352(6282), 224–227,
830 doi:10.1126/science.aad5300, 2016.
- 831 Taylor, K. E., Stouffer, R. J., Meehl, G. A., Taylor, K. E., Stouffer, R. J. and Meehl, G. A.: An
832 Overview of CMIP5 and the Experiment Design, *Bull. Am. Meteorol. Soc.*, 93(4), 485–498,
833 doi:10.1175/BAMS-D-11-00094.1, 2012.
- 834 Tebaldi, C. and Knutti, R.: The use of the multi-model ensemble in probabilistic climate
835 projections, *Philos. Trans. R. Soc. A Math. Phys. Eng. Sci.*, 365(1857), 2053–2075,
836 doi:10.1098/rsta.2007.2076, 2007.
- 837 Wang, D., Gouhier, T. C., Menge, B. A. and Ganguly, A. R.: Intensification and spatial
838 homogenization of coastal upwelling under climate change, *Nature*, 518(7539), 390–394,
839 doi:10.1038/nature14235, 2015.
- 840 Wenzel, S., Cox, P. M., Eyring, V. and Friedlingstein, P.: Emergent constraints on climate-
841 carbon cycle feedbacks in the CMIP5 Earth system models, *J. Geophys. Res. Biogeosciences*,
842 119(5), 794–807, doi:10.1002/2013JG002591, 2014.
- 843 Wenzel, S., Eyring, V., Gerber, E. P. and Karpechko, A. Y.: Constraining future summer austral
844 jet stream positions in the CMIP5 ensemble by process-oriented multiple diagnostic regression, *J.*
845 *Clim.*, 29(2), 673–687, doi:10.1175/JCLI-D-15-0412.1, 2016.
- 846

847

848 **APPENDIX**

849

Model-group 1	Model-group 2	Model-group 3	Model-group 4
ACCESS1-0 ACCESS1-3 CESM1-CAM5 CESM1-CAM5-1-FV2 CESM1-WACCM HadCM3 MIROC-ESM MIROC-ESM-CHEM MIROC5 NorESM1-M NorESM1-ME	bcc-csm1-1 bcc-csm1-1-m BNU-ESM CCSM4 CESM1-BGC CESM1-FASTCHEM GFDL-CM2p1 GFDL-ESM2G GFDL-ESM2M MPI-ESM-LR MPI-ESM-MR MPI-ESM-P	FGOALS-g2 GISS-E2-H GISS-E2-H-CC GISS-E2-R GISS-E2-R-CC inmcm4 IPSL-CM5A-LR IPSL-CM5A-MR IPSL-CM5B-LR MRI-CGCM3 MRI-ESM1	CanCM4 CanESM2 CMCC-CESM CMCC-CM <u>CMCC-CMS</u> <u>CNRM-CM5</u> <u>CNRM-CM5-2</u> CSIRO-Mk3-6-0 <u>FGOALS-s2</u> <u>GFDL-CM3</u> HadGEM2-AO HadGEM2-CC HadGEM2-ES

850

ZModel-group 1	ZModel-group 2	ZModel-group 3	ZModel-group 4
ACCESS1-0 bcc-csm1-1-m CCSM4 CESM1-BGC CESM1-CAM5 CESM1-CAM5-1-FV2 CESM1-FASTCHEM CESM1-WACCM GISS-E2-H GISS-E2-H-CC GISS-E2-R GISS-E2-R-CC HadCM3 inmcm4 IPSL-CM5B-LR MIROC5 MPI-ESM-LR MPI-ESM-MR MPI-ESM-P	<u>CMCC-CMS</u> <u>CNRM-CM5</u> <u>CNRM-CM5-2</u> <u>FGOALS-s2</u> <u>GFDL-CM3</u>	BNU-ESM CanCM4 CanESM2 CMCC-CM FGOALS-g2 IPSL-CM5A-LR IPSL-CM5A-MR MRI-CGCM3 NorESM1-M NorESM1-ME	ACCESS1-3 bcc-csm1-1 CSIRO-Mk3-6-0 HadGEM2-AO HadGEM2-CC HadGEM2-ES MIROC-ESM MIROC-ESM-CHEM MRI-ESM1
			ZModel-group 5
			CMCC-CESM GFDL-CM2p1 GFDL-ESM2G GFDL-ESM2M

851

852 Table A1: Composition of the different Model-groups identified in the main text. In bold, we
853 show the CMIP5 models which belong to Model-group 4 and ZModel-group 2. We note that all
854 the models belonging to Zmodel-group 2 also belong to Model-group 4.

855

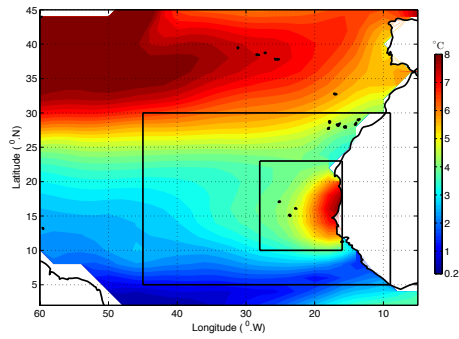
nb	Model Acronym	nb	Model Acronym
1	bcc-csm1-1	25	HadGEM2-ES
2	bcc-csm1-1-m	26	MPI-ESM-LR
3	BNU-ESM	27	MPI-ESM-MR
4	CanCM4	28	MPI-ESM-P
5	CanESM2	29	MRI-CGCM3
6	CMCC-CESM	30	MRI-ESM1
7	CMCC-CM	31	GISS-E2-H
8	CMCC-CMS	32	GISS-E2-H-CC
9	CNRM-CM5	33	GISS-E2-R
10	CNRM-CM5-2	34	GISS-E2-R-CC
11	ACCESS1-0	35	CCSM4
12	ACCESS1-3	36	NorESM1-M
13	CSIRO-Mk3-6-0	37	NorESM1-ME
14	inmcm4	38	HadGEM2-AO
15	IPSL-CM5A-LR	39	GFDL-CM2p1
16	IPSL-CM5A-MR	40	GFDL-CM3
17	IPSL-CM5B-LR	41	GFDL-ESM2G
18	FGOALS-g2	42	GFDL-ESM2M
19	FGOALS-s2	43	CESM1-BGC
20	MIROC-ESM	44	CESM1-CAM5
21	MIROC-ESM-CHEM	45	CESM1-CAM5-1-FV2
22	MIROC5	46	CESM1-FASTCHEM
23	HadCM3	47	CESM1-WACCM
24	HadGEM2-CC		

856

857 Table 1: List of the CMIP5 models used for the comparison. The reader is referred to the CMIP5
858 documentation for more information on each of them. Here, each configuration is furthermore
859 given a number, for easier identification in subsequent figures.

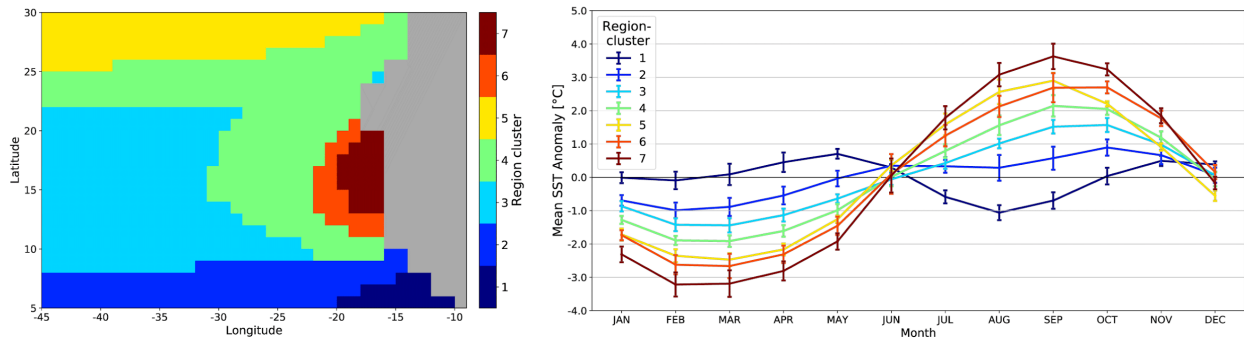
860

861



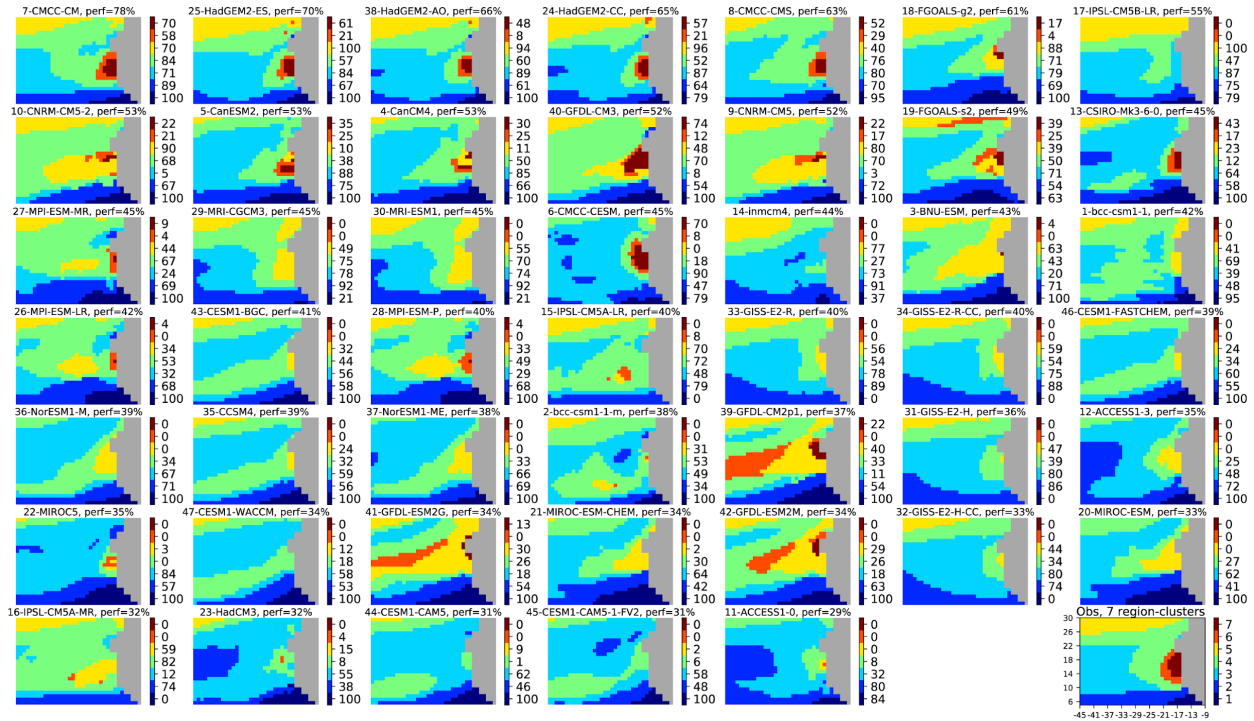
862

863 Figure 1: Amplitude of the SST seasonal anomalies in the western tropical north Atlantic. SST
864 data are from the ERSSTv3b data set averaged between 1975 and 2005. The two black boxes
865 show the extended and zoomed regions respectively, on which the statistical classifications were
866 performed (see text for details).
867



868

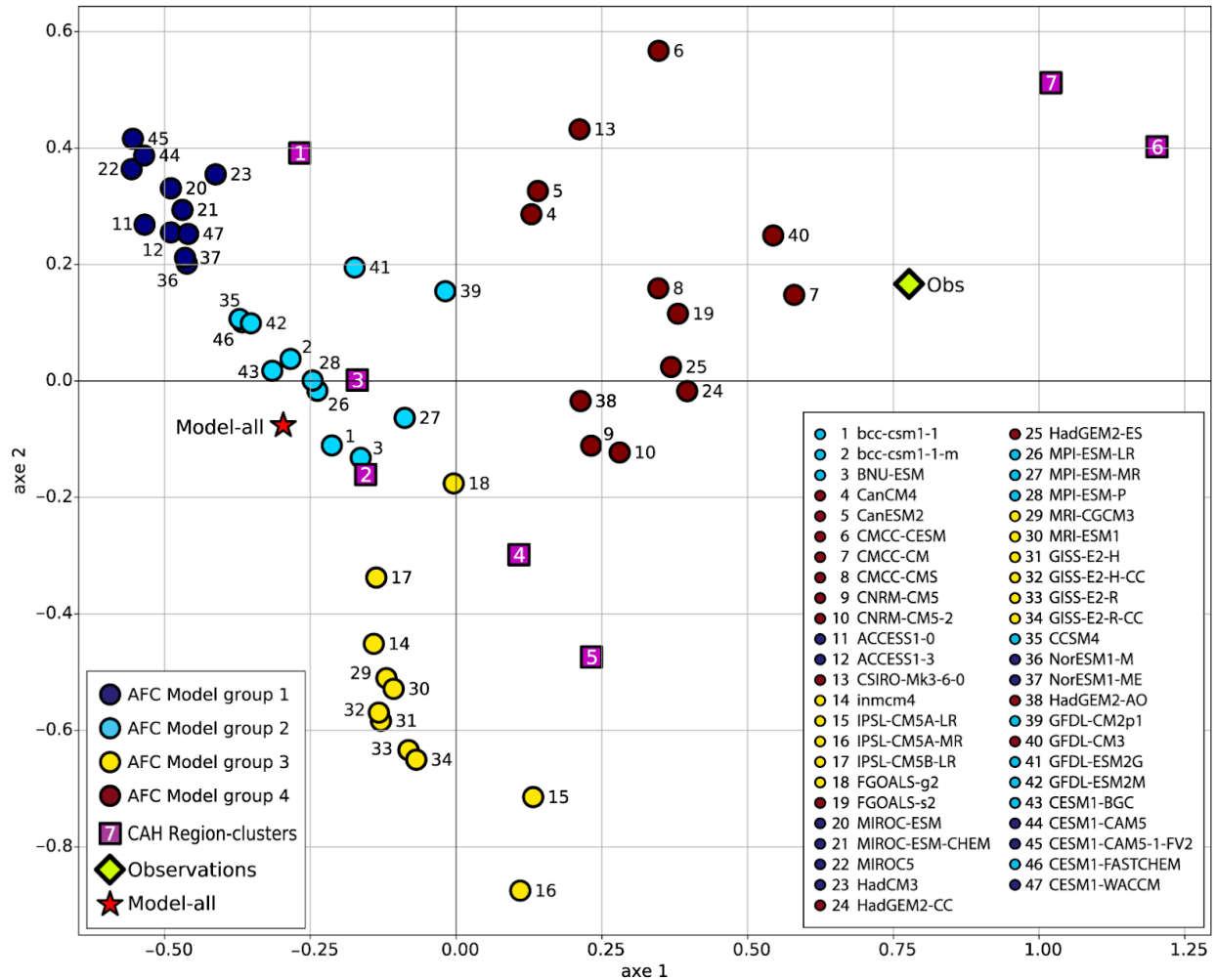
869 Figure 2: Left panel: Region-clusters associated with the SOM-clusters obtained after a HAC on
 870 a 30x4 neuron SOM learned on ERSSTv3b observations in the extended zone (see text for
 871 details). Right Panel: Ensemble-mean monthly climatological SST anomalies for the grid points
 872 of the seven Region-clusters. The error bars show the standard deviation of this ensemble mean.
 873



874

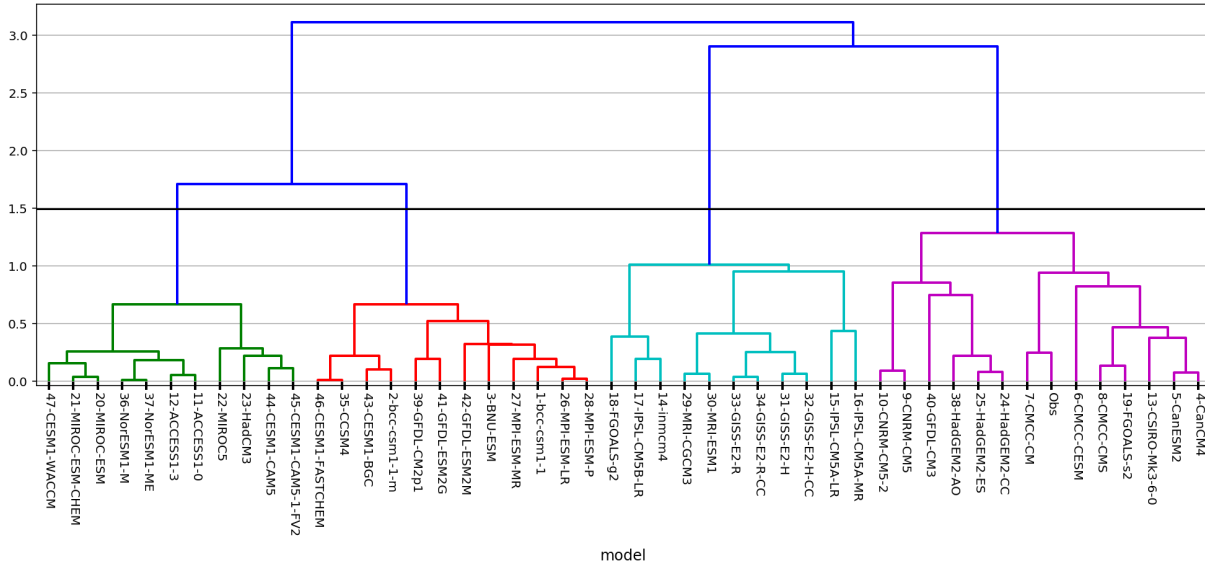
875

876 Figure 3: Projection of the 47 climate models of the CMIP5 database onto the SOM learned with
 877 ERSSTv3b climatology in the extended zone (see Fig. 1). On top of each panel, we figure: the
 878 number referencing the model, its name (Table 1), and its skill given as a mean percentage (see
 879 text). The models are ordered according to their skill in decreasing order. The 7 Region-clusters
 880 (or SOM-clusters) are defined by applying an HAC to the SOM output learned with the
 881 observation field. They are represented by different colors. The numbers in the colorbar at the
 882 right of each panel represent the skill for each Region-cluster. The observation field is shown in
 883 the bottom right panel and the numbers in front of the colorbar reference the Region-cluster.
 884



885

886 Figure 4: Projection of the CMIP5 models (colored circles) and the observation field (green
887 green diamond) defined by their cluster skill vectors on the first two axis of the MCA. The seven
888 region-clusters of the observation field are represented by purple squares. The colours of the
889 circles denote the four groups of models obtained after an HAC was performed on the seven
890 MCA components of the models. The projection of the full multi-model mean (47 models) is
891 represented by a red star. We note that some bias can be introduced in this projection since the
892 projection on the other axes can be of importance
893



894

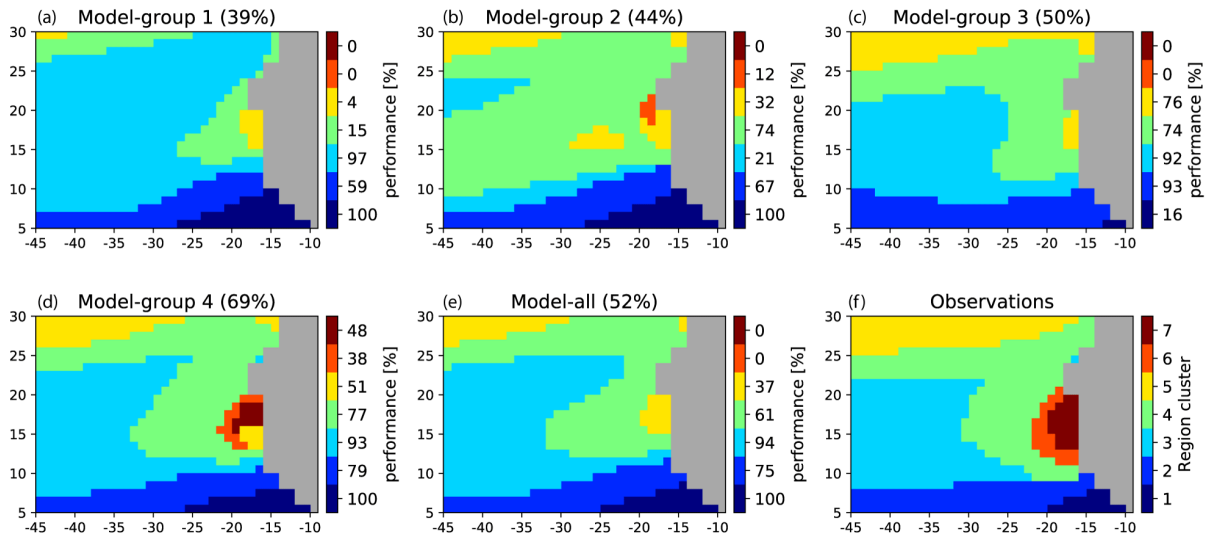
895

896 Figure 5: HAC Dendrogram. The horizontal line displays the 47 CMIP5 models, each model
 897 being associated with its 7 component skill-vector. As the dendrogram represents a hierarchy of
 898 clusters, the numbers on the y axis give the distance between two clusters. We note an optimal
 899 'jump' on this graph: the level 1.5 in the vertical axis (materialized by a horizontal black line) is
 900 associated with 4 well-separated clusters corresponding to 4 Model-groups that are very different.

901

902

903

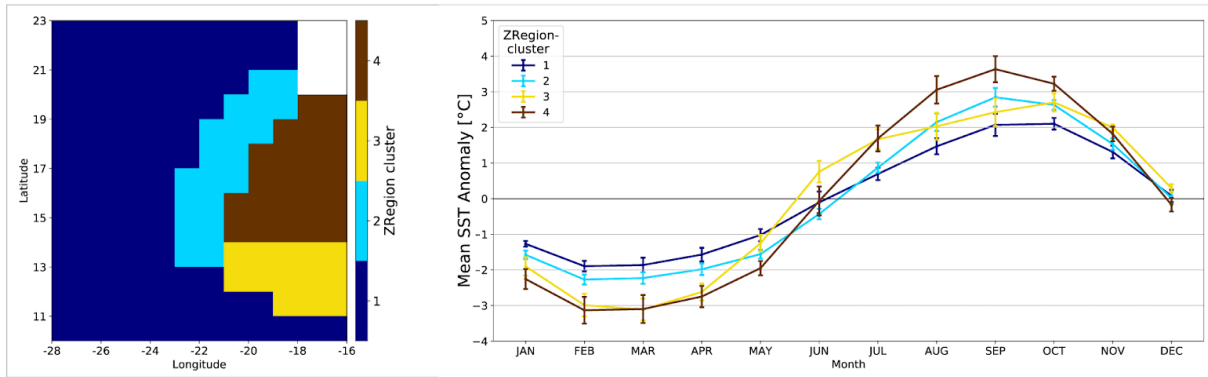


904

905 Figure 6: (a)-(d): Projection of the multi-model ensembles (Model-group) onto the SOM learned
 906 with ERSSTv3b climatology in the extended zone. Multi-model ensemble performances are
 907 obtained by averaging the skill of the models forming each group. The performances are given
 908 on top of each panel. The Region-clusters determined by processing the observations in the
 909 extended area and their associated colors are given in the bottom right panel. The colorbars at the
 910 right of each multi-ensemble panel represent the skill (in %) associated with each Region-cluster.
 911 Panel (e) shows the projection for the full multi-model ensemble. Panel (f) reproduces the
 912 Region-clusters based on the observations also shown in Fig. 2.

913

914



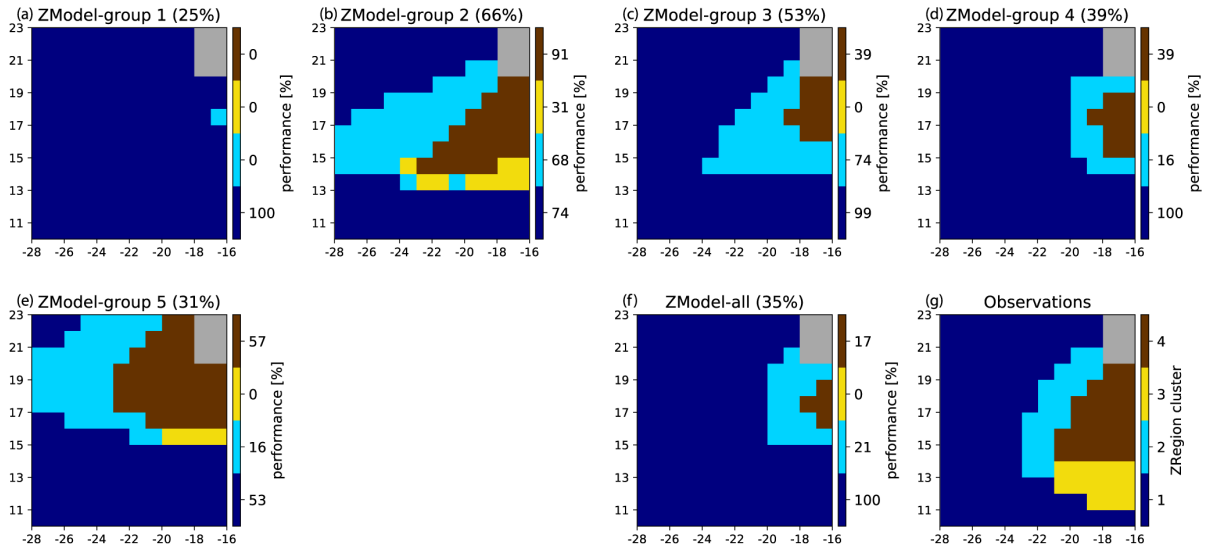
915

916 Figure 7: Left panel: ZRegion-clusters associated with the ZSOM-clusters obtained after a HAC
 917 on a 10x12 neuron SOM learned on ERSSTv3b observations in the zoomed zone (see text for
 918 details). Right Panel: Ensemble-mean monthly climatological SST anomalies for the grid points
 919 of the four ZRegion-clusters. The error bars show the standard deviation of this ensemble mean.

920

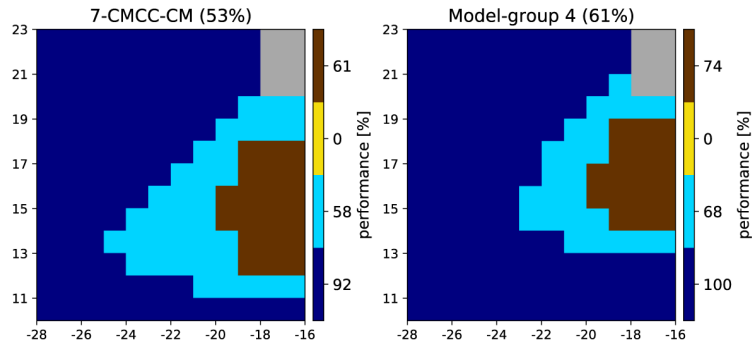
921

922



923

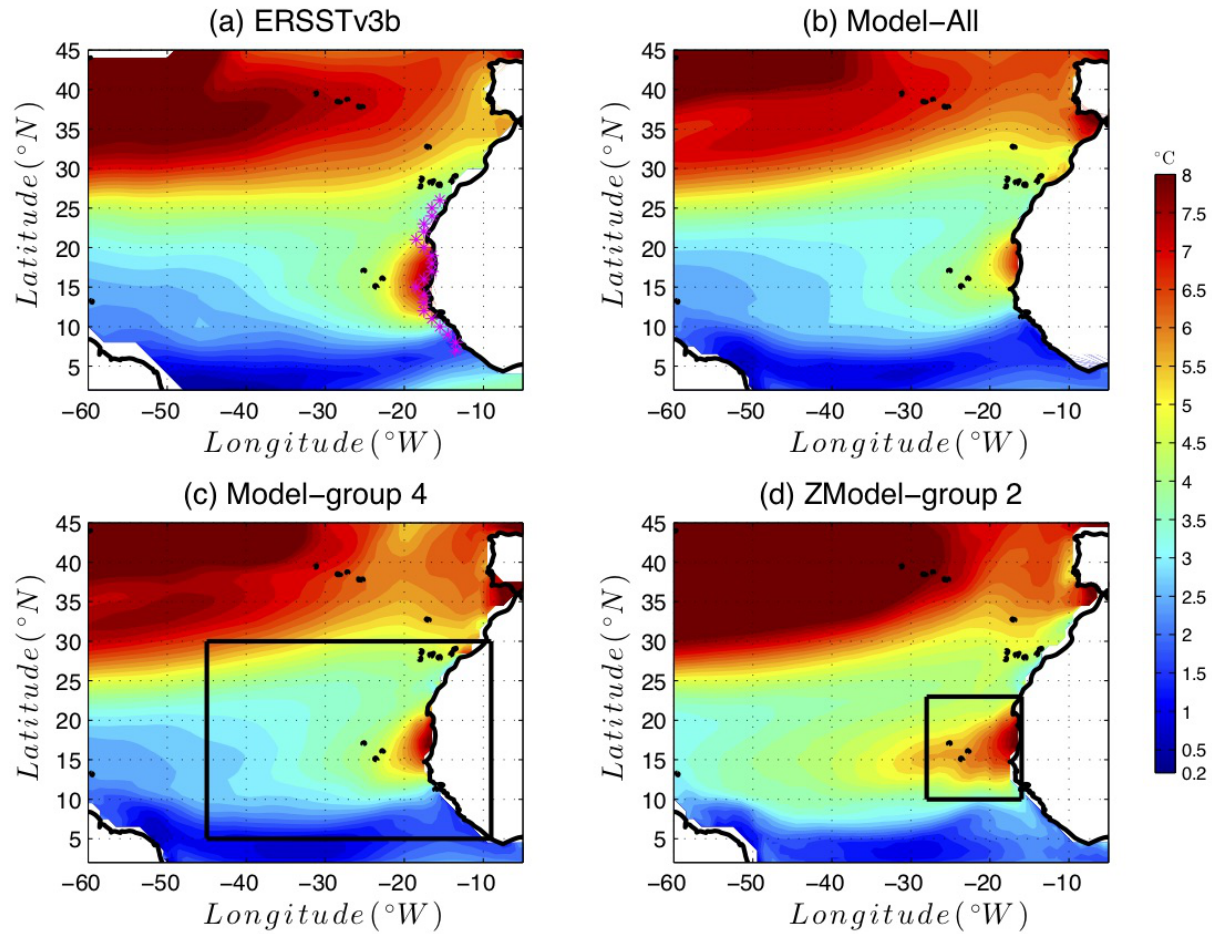
924 Figure 8: (a)-(e): Projection of the multi-model ensembles (*ZModel*-groups) onto the *ZSOM*. The
 925 performances are given on top of each panel. The *ZRegion*-clusters determined by processing the
 926 observations in the zoomed region and their associated colors are given in the bottom right panel.
 927 The colorbars at the right of each multi-ensemble panel represent the skill (in %) associated with
 928 each *ZRegion*-cluster. Panel (f) shows the same for the full multi-model ensemble. Panel (g)
 929 reproduces the *Region*-clusters based on the observations also shown in Fig. 6.
 930



931

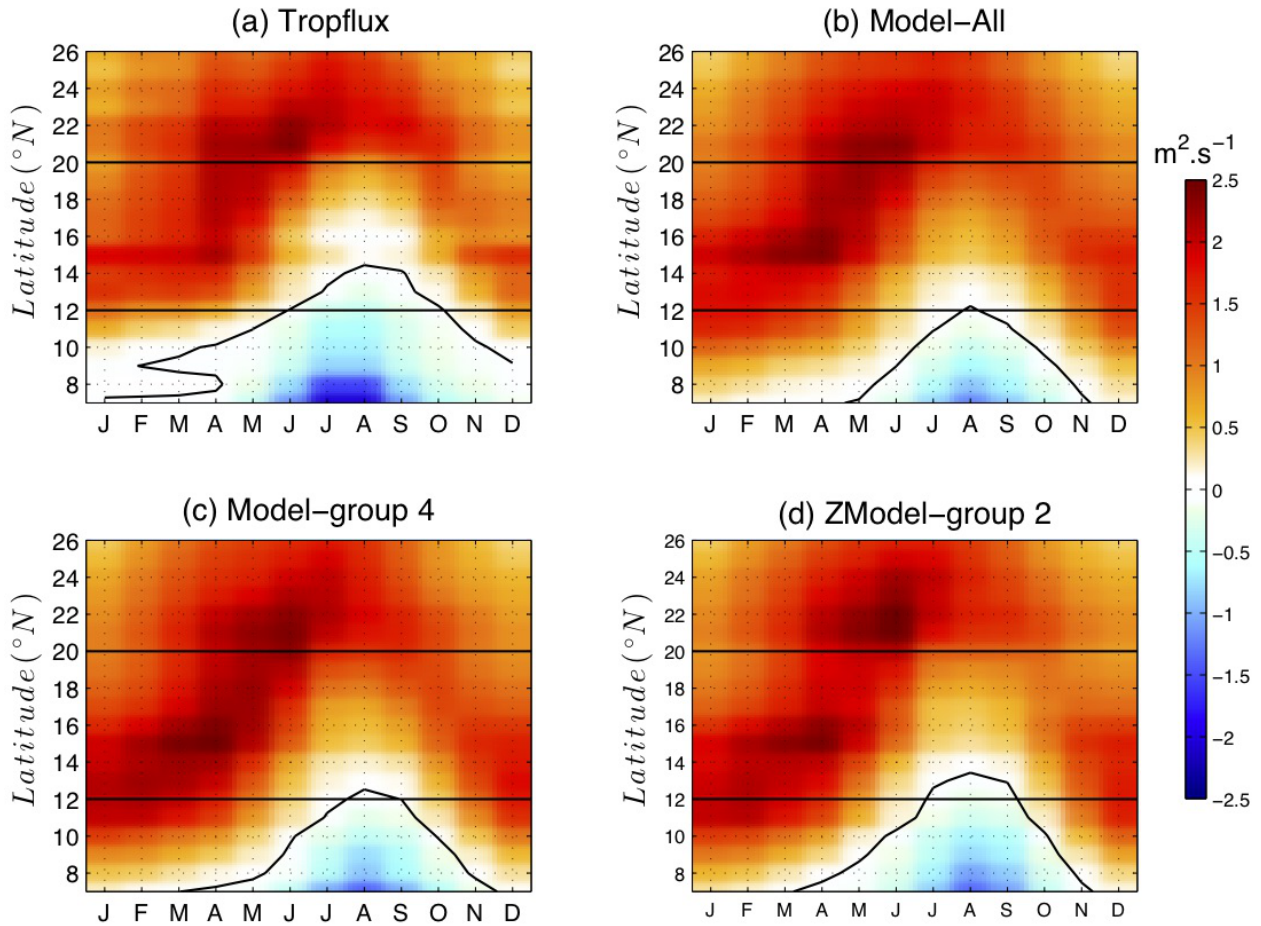
932 Figure 9 : Same as Fig. 7 but for the individual model CMCC-CM (model 7) (left) and the
933 Model-group 4 (right).

934



935

936 Figure 10: Amplitude of the SST seasonal cycle in the (a) ERSSTv3b Observations (b) Model-
 937 All, c) Model-group 4 (best Model-group for the extended area, figured out by the black
 938 rectangular box) and (d) ZModel-group 2 (best Model-group for the reduced area, figured out by
 939 the small black rectangular box). The SST seasonal cycle is computed over the period 1985-2005
 940

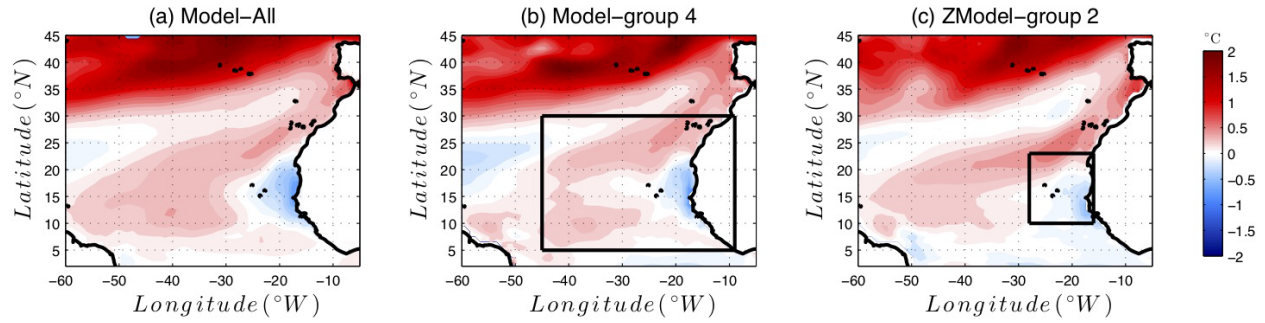


941

942 Figure 11: Latitude-time plot of depth integrated Ekman transport computed over the grid point
 943 located along the coast (magenta stars in Fig. 9.a). The time axis shows climatological months
 944 over the period 1985-2005. Positive (negative) values correspond to upwelling (downwelling)
 945 conditions. Panel (a) stands for TropFlux data set (see (Praveen Kumar et al., 2011) (b) Model-
 946 All, (c) Model-group 4 and (d) ZModel-group 2. In each panel, the black contour shows the
 947 contour zero. The horizontal dashed lines are positioned at 12 $^{\circ}N$ and 20 $^{\circ}N$ and give a rough
 948 limitation of the Senegalo-Mauritanian upwelling region.

949

950

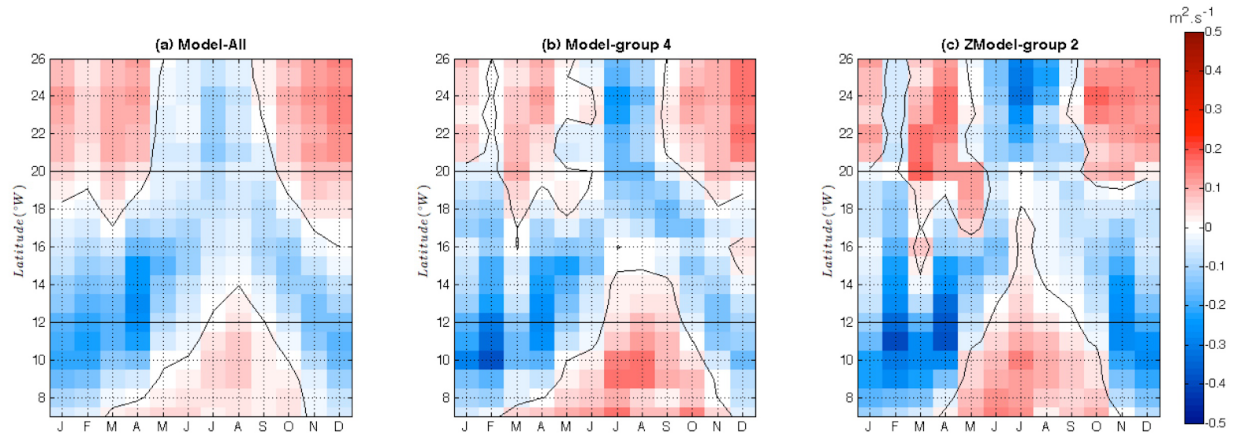


951

952 Figure 12: Evolution of the amplitude of the SST seasonal cycle at the end of the 21st century.
 953 The figure shows the difference between the seasonal cycle amplitude averaged over the period
 954 [2080-2100] following the RCP8.5 scenario and the amplitude averaged over the period [1985-
 955 2005] in the historical simulations. A positive value (red) means that the seasonal cycle is more
 956 marked over the period 2080-2100.

957

958



959

960 Figure 13: Latitude-time diagram of the seasonal shift of the meridional component of the wind-
 961 stress with respect to the present days. For each month and at each latitude, we show the
 962 meridional wind stress shift with respect to the present days averaged over the period [2080-
 963 2100]. Positive values (red) means that the wind stress shift is southward and is thus favorable to
 964 upwelling. Panel (a) stands for Model-All, (b) Model-group 4 and (c) ZModel-group 2.
 965